THE ASTROPHYSICAL JOURNAL, 808:146 (21pp), 2015 August 1 doi:10.1088/0004-637X/808/2/146

SHORT- AND LONG-TERM RADIO VARIABILITY OF YOUNG STARS IN THE ORION NEBULA CLUSTER AND MOLECULAR CLOUD

V. M. RIVILLA[1,2], C. J. CHANDLER[3], J. SANZ-FORCADA[4], I. JIMÉNEZ-SERRA[5,6], J. FORBRICH[7], AND J. MARTÍN-PINTADO[1]
[1] Osservatorio Astrofisico di Arcetri, Largo Enrico Fermi 5, I-50125, Firenze, Italy; rivilla@arcetri.astro.it
[2] Centro de Astrobiología (CSIC/INTA), Ctra. de Torrejón a Ajalvir km 4, E-28850 Torrejón de Ardoz, Madrid, Spain
[3] National Radio Astronomy Observatory, P.O. Box O, Socorro, NM 87801, USA
[4] Centro de Astrobiología (CSIC/INTA), ESAC Campus, P.O. Box 78, E-28691 Villanueva de la Cañada, Madrid, Spain
[5] European Southern Observatory, Karl-Schwarzschild-Str. 2, D-85748, Garching, Germany
[6] Department of Physics and Astronomy, University College London, 132 Hampstead Road, London NW1 2PS, UK
[7] Department of Astrophysics, University of Vienna, Türkenschanzstr. 17, 1180 Vienna, Austria
Received 2014 June 4; accepted 2015 April 3; published 2015 July 29

ABSTRACT

We have used the Karl G. Jansky Very Large Array (VLA) to carry out multi-epoch radio continuum monitoring of the Orion Nebula Cluster (ONC) and the background Orion Molecular Cloud (OMC; 3 epochs at Q band and 11 epochs at Ka band). Our new observations reveal the presence of 19 radio sources, mainly concentrated in the Trapezium Cluster and the Orion Hot Core (OHC) regions. With the exception of the Becklin–Neugebauer object and source C (which we identify here as dust emission associated with a proplyd) the sources all show radio variability between the different epochs. We have found tentative evidence of variability in the emission from the massive object related to source I. Our observations also confirm radio flux density variations of a factor >2 on timescales of hours to days in five sources. One of these flaring sources, OHC-E, has been detected for the first time. We conclude that the radio emission can be attributed to two different components: (i) highly variable (flaring) non-thermal radio gyrosynchrotron emission produced by electrons accelerated in the magnetospheres of pre-main-sequence low-mass stars and (ii) thermal emission due to free–free radiation from ionized gas and/or heated dust around embedded massive objects and proplyds. Combining our sample with other radio monitoring at 8.3 GHz and the X-ray catalog provided by *Chandra*, we have studied the properties of the entire sample of radio/X-ray stars in the ONC/OMC region (51 sources). We have found several hints of a relation between the X-ray activity and the mechanisms responsible for (at least some fraction of) the radio emission. We have estimated a radio flaring rate of ~0.14 flares day^{-1} in the dense stellar cluster embedded in the OHC region. This suggests that radio flares are more common events during the first stages of stellar evolution than previously thought. The advent of improved sensitivity with the new VLA and ALMA will dramatically increase the number of stars in young clusters detected at radio wavelengths, which will help us improve our understanding of the origin and nature of the radio emission.

Key words: stars: flare – stars: formation – stars: low-mass – stars: protostars – radio continuum: stars – X-rays: stars

Supporting material: FITS file

1. INTRODUCTION

High-energy processes during the first evolutionary stages of star formation are responsible for both radio and X-ray emission (Feigelson & Montmerle 1999). Low-mass pre-main-sequence (PMS) stars are well-known strong X-ray emitters. Their enhanced magnetic activity with respect to more evolved stars produces violent reconnection events in the corona of the stars, where the plasma heated to high temperatures strongly emits variable X-ray emission. Massive stars also emit X-ray radiation, usually related to wind shocks.

Our understanding of the X-ray emission from young stars has dramatically increased in recent years due to *Chandra* and *XMM-Newton* (Arzner et al. 2007; Getman et al. 2008). X-ray observations have revealed thousands of PMS stars in tens of stellar clusters, resulting in good constraints on their X-ray properties such as plasma temperatures, levels of variability, luminosities, and X-ray flare rates (see, e.g., Wolk et al. 2005).

In contrast, the physics associated with the radio events (nature and origin of the emission, variability, timescales, flaring rate) are still poorly constrained. Drake & Linsky (1989) proposed that radio flares might be produced by the same coronal activity that is responsible for bright X-ray emission (see review by Güdel 2002). It would be expected then that electrons spiraling in the magnetic field of the corona produce non-thermal and highly variable gyrosynchrotron radiation. Moreover, ionized material in the vicinity of stars, in circumstellar disks or envelopes or at the base of bipolar outflows, also produce thermal free–free (*bremsstrahlung*) radiation.

Long-term radio variability on timescales of months to years has been observed in star-forming regions (Felli et al. 1993; Zapata et al. 2004; Forbrich et al. 2007; Choi et al. 2008). However, it is still not clear whether these variations are caused by long-term mechanisms or they are indeed produced by a sequence of events occurring on shorter timescales. Systematic observations looking for short-term variability are required to answer this question.

Recently, Liu et al. (2014) detected radio variability on hour timescales in the young stellar cluster R Coronae Australis. The most powerful radio flares[8] have been serendipitously reported

[8] In this work we will use the term *flare* to refer to flux density variations of a factor of >2 on timescales from hours to days.

Table 1
Multi-epoch VLA Radio Continuum Observations

Config.	Project ID	Band Name	Freq. (GHz)	BW (MHz)	Epoch	JD	Pointing Center		Obs. Length (minutes)	Beam ($'' \times ''$)	rms (mJy)	Primary Flux Density Calibrator	Gain Calibrator Flux Density (Jy) (J0541–0541)
							R.A.$_{J2000}$ 5h 35m	Decl.$_{J2000}$ -5^{o} $22'$					
B	AJ356	Q	45.6	25	2009 Mar 9	2454900	$14^{s}.60$	$30''.0$	120	0.23×0.15	0.45	J0137 + 3309	0.63
B	AJ356	Q	45.6	25	2009 Mar 19	2454910	$14^{s}.60$	$30''.0$	240	0.22×0.15	0.37	J0137 + 3309	0.63
D	AR712	Q	43.3	100	2009 Dec 22	2455188	$14^{s}.50$	$31''.0$	60	1.9×1.4	0.54	J0137 + 3309	0.46
C	10B-175	Ka	33.6	256	2010 Oct 24	2455494	$14^{s}.50$	$30''.0$	30	1.3×0.65	0.36	J0542 + 4951	0.68
C	10B-175	Ka	33.6	256	2010 Nov 23	2455523.76	$14^{s}.50$	$30''.0$	30	0.92×0.60	0.40	J0542 + 4951	0.68
C	10B-175	Ka	33.6	256	2010 Nov 23	2455523.89	$14^{s}.50$	$30''.0$	30	0.75×0.56	0.44	J0137 + 3309	0.69
C	10B-175	Ka	33.6	256	2011 Jan 8	2455569	$14^{s}.50$	$30''.0$	30	0.86×0.56	0.39	J0137 + 3309	0.62
CnB-B	10B-175	Ka	33.6	256	2011 Feb 8	2455601	$14^{s}.50$	$30''.0$	30	0.30×0.24	0.32	J0137 + 3309	0.58
B	10B-175	Ka	33.6	256	2011 Mar 28	2455649	$14^{s}.50$	$30''.0$	30	0.28×0.22	0.22	J0542 + 4951	0.50
BnA	10B-175	Ka	33.6	256	2011 May 27	2455709	$14^{s}.50$	$30''.0$	30	0.62×0.077	0.22	J0542 + 4951	0.54
BnA-A	10B-175	Ka	37.5	128	2011 Jun 4	2455717	$14^{s}.50$	$30''.0$	120	0.096×0.073	0.13	J0542 + 4951	0.50
BnA-A	10B-175	Ka	30.5	128	2011 Jun 4	2455717	$14^{s}.50$	$30''.0$	120	0.13×0.083	0.10	J0542 + 4951	0.52
A	10B-175	Ka	33.6	256	2011 Jun 11	2455724	$14^{s}.50$	$30''.0$	30	0.14×0.062	0.16	J0137 + 3309	0.54
A	10B-175	Ka	33.6	256	2011 Jul 09	2455752	$14^{s}.50$	$30''.0$	30	0.091×0.060	0.14	J0542 + 4951	0.48

so far toward the Orion Nebula Cluster (ONC) and the background Orion Molecular Cloud (OMC). Bower et al. (2003) reported a strong radio flare at 86 GHz arising from a PMS star in the ONC, and Forbrich et al. (2008) presented an even stronger radio flare at 22 GHz, originating from a young star deeply embedded in the OMC previously detected through its X-ray emission. The low number of observed events could indicate that radio flares are a rare phenomenon (Andre et al. 1996) but at the same time prevents a proper statistical analysis of short-term variability phenomena.

Since the typical timescales of radio variability are poorly known, we have carried out a monitoring program comprised of various cadences ranging from 3 hr to several months. The new capabilities of the Karl G. Jansky Very Large Array (JVLA) now allow the scheduling of multiple, short snapshots with good sensitivity in a reasonable amount of observing time. The only two examples of powerful radio flares are located in Orion, and this region also harbors a rich cluster of low-mass stars (Rivilla et al. 2013a); hence, this region is an excellent target for the detection of many sources in a single pointing.

We have carried out a multi-epoch radio continuum monitoring of the ONC/OMC region using the Karl G. Jansky VLA. This is the first radio monitoring at high centimeter frequencies in Orion, with three epochs at Q band and 11 epochs at Ka band. Our data allow us to study for the first time both the short (hours to days) and long (months) timescale variability of the radio sources in Orion.

The paper is laid out as follows. In Section 2 we present the details of the observations. In Section 3 we show the results of the monitoring at Ka and Q bands. In Section 4 we compare our results with a previous monitoring at lower frequency (8.3 GHz). We also compile the full sample of radio/X-ray sources in the ONC/OMC region, and then compare the radio and X-ray properties with the aim of better understanding the link between radio and X-ray emission. In Section 5 we discuss in more detail the new radio flaring source detected by our monitoring, OHC-E. In Section 6 we analyze in particular the radio variability observed in the binary system θ^1 Ori A. In Section 7 we estimate the rate of radio flaring activity of young stars in the Orion Hot Core (OHC). Finally, in Section 8 we summarize the conclusions of our work.

2. OBSERVATIONS AND DATA REDUCTION

The radio observations of the ONC/OMC region were made with the VLA in the A, B, C, and D configurations at Q band (three epochs) and Ka band (11 epochs) from 2009 to 2011. Table 1 summarizes the observational details for each of the epochs: array configuration, project ID, band name, frequency, observing bandwidth, date, pointing center, observation length (including all calibrations), synthesized beam, rms noise at the center of the primary beam, primary flux density calibrator used, and the flux density of the complex gain calibrator. The separation between the epochs is different: the shortest one is only 3 hr, others are separated by several days, and some others by several months. This will allow us to trace radio variability at different timescales. The first two observations at Q band (45.6 GHz) were made in spectral line mode using the old VLA correlator, single polarization. The third Q-band observation (45.6 GHz, AR712) used the standard dual polarization continuum setup with the old correlator (100 MHz total bandwidth). For the data taken under observing code 10B-175 the new WIDAR correlator was used, with two 128 MHz sub-bands centered on 33.56 GHz placed contiguously in frequency for all observations except those of 2011 June 4, for which the sub-bands were separated by 7 GHz as noted in Table 1. The observations at Q-band were reduced using the AIPS package. The observations at Ka-band were reduced using the VLA Calibration Pipeline[9], which uses the Common Astronomy Software Applications (CASA) package.[10]

Phase self-calibration was performed where possible. However, the tropospheric phase stability of the observations on 2011 June 4 was poor, and the data were of insufficient signal-to-noise ratio to enable phase self-calibration on short enough timescales to correct for the resulting decorrelation. While the typical uncertainty in the absolute flux density scale is 10% at these frequencies, the uncertainty in the absolute flux density scale for the 2011 June 4 data increased to 20%. Images were made using CASA, applying an inner uv-cutoff (>50 kλ) to filter the extended emission from the foreground H II region ionized by the Trapezium cluster, and natural weighting to maximize sensitivity. The images are corrected for the response of the primary beam before being used for photometry. The FITS files of the reduced images are available in the HTML version of the journal.

3. RESULTS: RADIO STELLAR POPULATION DETECTED AT HIGH CENTIMETER FREQUENCIES

The large fields of view (FOVs) covered by the images made here, especially in the VLA's B and A configurations, require a rigorous criterion for the detection of sources. Assuming Gaussian noise, and approximating the number of potential sources as the ratio between the area of the FOV and the solid angle of the beam ($\pi\theta_{\rm minor}\theta_{\rm major}/4{\rm Ln}2$), we would expect <0.3 sources above five times the local rms noise (5σ) in the worst case. Therefore, we only report detections with flux densities $>5\sigma$.

We detected a total of 19 sources (Table 2), 18 of which have been previously detected by the radio monitorings at lower frequencies (Felli et al. 1993 at 5 and 15 GHz and Zapata et al. 2004 at 8.3 GHz). Our observations have revealed the presence of a new radio source, hereafter OHC-E, detected in the OHC region in two different epochs. In Figure 1 we show the positions of all the detected sources, overplotted on the R-band Advanced Camera for Surveys/Wide Field Channel (ACS/WFC) *Hubble Space Telescope* (*HST*) image and on the infrared K-band image from the 2MASS. The sources are mainly concentrated in the OHC region and the Trapezium Cluster, which harbors the two highest stellar densities within our FOV (Rivilla et al. 2013a).

To measure the flux densities of the sources, we use the AIPS task JMFIT.[11] We also add an absolute uncertainty of 10% in quadrature (20% for the 2011 June 4 observations due to the poorer phase stability of those data; see Section 2). Table 3 summarizes the results. Only the sources Becklin–Neugebauer (BN) and source I are detected in all epochs, showing nearly constant flux densities, and verifying the reproduceability of the flux density scale. Source C is consistent with a constant flux density, although is not detected in all epochs. The other sources exhibit clear flux density

[9] https://science.nrao.edu/facilities/vla/data-processing/pipeline
[10] http://casa.nrao.edu
[11] JMFIT fits a two-dimensional Gaussian models to the sources by least-squares.

Table 2
Positions of the Radio Sources Detected in Our Ka-Band and Q-Band Monitoring

Source	R.A.$_{J2000}$ 5 35	Decl.$_{J2000}$ −5
BN	14.11	22 22.69
I	14.51	22 30.58
OHC-E	14.73	22 29.83
D	14.90	22 25.38
n[a]	14.35	22 32.89
H	14.50	22 38.76
A	11.80	21 49.29
C	14.16	23 01.04
F	18.37	22 37.43
G	17.95	22 45.42
E	16.96	22 48.78
15	16.07	23 07.12
6	16.75	23 16.44
7	16.28	23 16.58
25	15.77	23 09.86
12	15.82	23 14.00
11	15.84	23 22.40
16	16.33	23 22.54
5	16.85	23 26.31

Note.
[a] This source was called *L* by Garay (1987), but its more common name is n (Menten & Reid 1995).

variation between epochs. In the case of non-detections, we quote 3σ upper limits.

3.1. Long-term Variability: Month Timescales

In this section we study the behavior of the radio emission throughout the full monitoring. In Figures 2 and 3 we show the measured integrated flux densities of all sources during the different epochs of our monitoring for the Q band and Ka band, respectively. We note that in the figures the observation on JD 2455188 (2009 December 22) at Q band corresponds to a slightly different frequency (43.3 GHz) from the first two epochs (45.6 GHz). Also, the flux density from the observation on JD 2455717 (2011 June 4) at Ka band (shown in Figure 3) corresponds to 30.5 GHz, and not to 33.6 GHz as for the others.

With the aim of quantifying the radio variability, we study two parameters: (i) the standard deviation ΔF of the flux densities from the average flux $F_{\rm av}$, which measures the absolute variability; and (ii) β, which is defined as $\beta = \Delta F/F_{\rm av}$, following Felli et al. (1993), which measures the relative variability. Given that some sources remain undetected in some epochs, and hence have flux densities below the sensitivity limit, we consider in the calculation of ΔF (and hence of β) the positive detections as well as the lowest upper limit. In Table 4 we show the values of $F_{\rm av}$, ΔF, and β for the sources detected.

The sources BN and I are associated with massive stars (Reid et al. 2007; Goddi et al. 2011), and are expected to emit mainly thermal (and constant) emission arising from ionized gas surrounding the central object. Our monitoring at Q band and Ka band (Figures 2 and 3) shows indeed that the flux density of BN is nearly constant, with a very low month-timescale radio variability parameter at 33.6 GHz of $\beta = 0.06$.

In the case of source I the radio variability is higher, $\beta = 0.13$. Zapata et al. (2004) also reported some variability toward this source, with flux density variations of a factor ∼2. Furthermore, Plambeck et al. (2013), using observations separated by 15 yr also found evidence of a gradual flux density increase from source I with respect to the more steady flux density of BN (see their Figure 5). From our Ka-band monitoring, we have studied the month-timescale evolution of the ratio between the flux densities of sources I and BN. Figure 4 shows that this ratio exhibits variations larger than the statistical uncertainties (we do not include the uncertainty in the absolute flux density scale in calculating the error in these ratios), suggesting that real variability is present. The origin of this confirmed long-term variability toward source I could be due to ionization of infalling accretion flows onto the massive star (Galván-Madrid et al. 2011; De Pree et al. 2014).

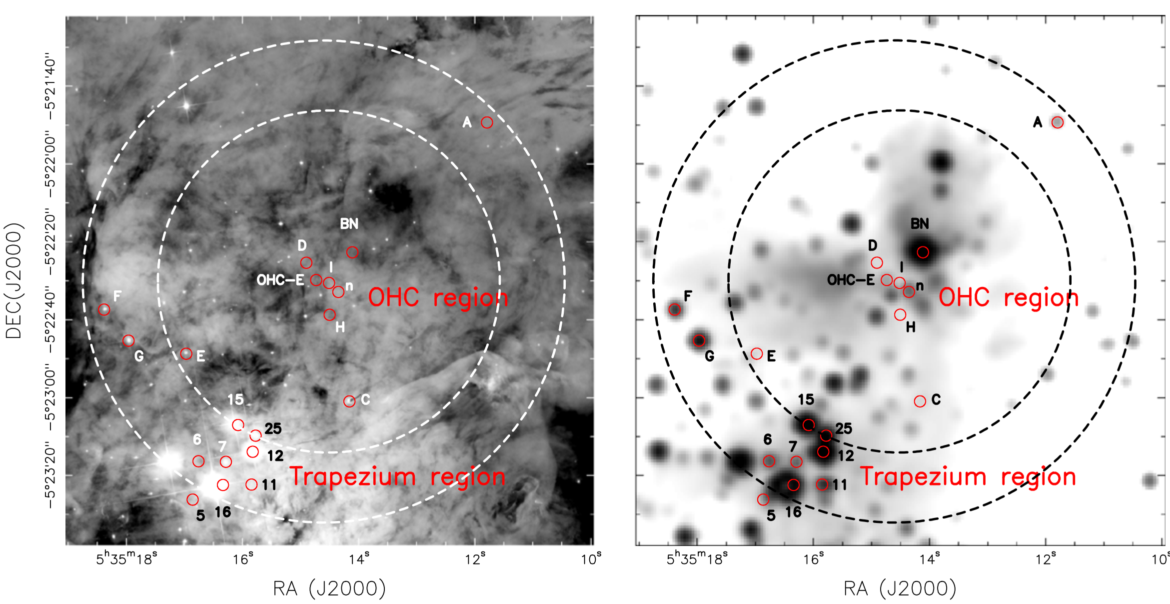

Figure 1. Position of the 19 radio sources detected in our monitoring program, overplotted on the R-band ACS/WFC *HST* image (left panel) and on the K-band two Micron All Sky Survey (2MASS) image (right panel). The dotted circles indicate the regions of the field where the primary beam responses are >0.15 at Q band (43.3 GHz) and Ka band (33.6 GHz).

Source C is only detected in the epochs for which the VLA was in its most compact configurations. This suggests that the emission from source C is extended, and that the higher resolution observations have filtered it out. To derive a proper sensitivity level for extended emission we have smoothed the B-configuration images at Q band to the resolution of the D-configuration image ($1''.9 \times 1''.4$). For the Ka-band monitoring, we have smoothed the higher resolution images (from 2011 February 8 to 2011 July 09) to a C-configuration resolution of $0''.8 \times 0''.8$. We have inspected the smoothed images, and measured the flux density (or 3σ upper limit) at the location of source C. The resulting light curves (Figures 2 and 3) are in agreement with nearly constant emission during the monitoring. This radio source is associated with one of the proplyds[11] revealed by *HST* (see Figure 5). Using the flux densities detected at 33.6 and 43.3 GHz, we obtain a spectral index ($F \sim \nu^{\alpha}$) of $\alpha \sim 3$, consistent with optically thin dust emission from the proplyd.

The other sources detected show clear variations at Ka band between epochs ($\beta > 0.29$). Many of them are detected only in some epochs, remaining below the sensitivity limit at other epochs. There is no clear trend or pattern in the variability, which appears to be stochastic for many of the sources. This highly variable emission suggests non-thermal processes. Indeed, Menten et al. (2007) detected four of these sources (A, F, G, and 12) with Very Long Baseline Array observations, confirming their compactness and hence the non-thermal nature of the emission.

Using epochs separated by ~1 month, it is not possible to determine whether flux density variation is smooth during this period, or whether it happens in shorter timescales. Observations with shorter separations are needed. We address this issue in Section 3.2.

3.2. *Short-term Variability*

3.2.1. *Day Timescales*

The first two Q-band observations are only separated by 10 days (2009 March 9 and 19). The main result obtained by comparing these observations is the discovery of a new radio source (hereafter OHC-E). Figure 6 shows the comparison of the two images. The source is detected at $3''.3$ northeast of source I. The flux density variation between the two epochs is >5.6 (using the 3σ upper limit as the flux density in the 2009 March 9 image). Source OHC-E shows a constant flux density during the four hours of the 2009 March 19 observation, indicating that we might have detected a fraction of a powerful flare event. This is consistent with the duration reported on other radio flares observed in Orion (source A and ORBS), which have timescales of hours to days.

3.2.2. *Hour Timescales*

Two of the Ka-band observations are separated by only ~3 hr (2010 November 23), enabling the study of flux density variations on even shorter timescales. Figure 7 shows the flux density variation of the 10 sources detected in these two epochs, normalized by the flux density of BN. In Table 5 we show the ratio between the flux densities of the two epochs ($F_{523.89}/F_{523.76}$, where the subscript is the JD date minus

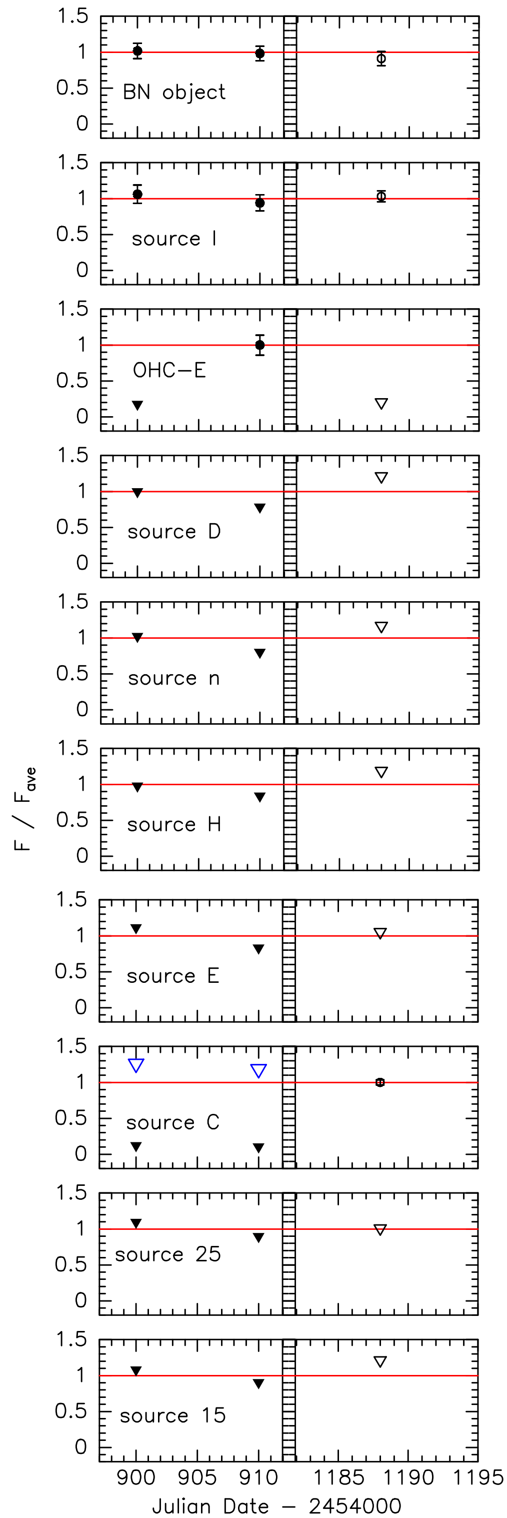

Figure 2. Q-band light curves for those sources that fall within the Q-band primary beam. In the case of non-detections, 3σ upper limits are indicated with triangles. The flux densities have been normalized by the average value (F_{av}) calculated with the positive detections (or the average value of the upper limits if the source is not detected). The error bars indicate the flux density uncertainties. The red horizontal line indicates the value at which the flux density is equal to the average. The first two observations were carried out at 45.6 GHz (black filled symbols), while the last one was carried out at 43.3 GHz (black open symbols). For source C, the blue open triangles indicate upper limits for extended emission derived from smoothed images (see Section 3.1).

[11] Proplyds are objects for which circumstellar material is being ionized by the ultraviolet radiation from massive stars.

Table 3
Multi-epoch Radio Continuum Flux Densities[a]

Source	Epoch: JD—2454000													
	900	910	1188	1494	1523.76	1523.89	1569	1601	1649	1709	1717		1724	1752
	Q-band (GHz)			Ka-band (GHz)										
	45.6	45.6	43.3	33.6	33.6	33.6	33.6	33.6	33.6	33.6	37.5	30.5	33.6	33.6
BN	31.2 ± 3.3	30.1 ± 3.1	27.9 ± 3.0	26.4 ± 2.7	25.9 ± 2.7	27.2 ± 2.8	23.9 ± 2.5	24.6 ± 2.5	25.7 ± 2.6	27.8 ± 2.8	20.5 ± 4.1	18.8 ± 3.8	25.7 ± 2.6	22.7 ± 2.3
I	14.1 ± 1.7	12.5 ± 1.5	13.7 ± 1.7	9.2 ± 1.1	9.1 ± 1.2	12.5 ± 1.5	10.7 ± 1.3	10.8 ± 1.2	9.7 ± 1.1	9.3 ± 1.0	9.1 ± 1.9	7.3 ± 1.5	10.8 ± 1.2	8.1 ± 0.9
OHC-E	(1.4)	7.9 ± 1.1	(1.6)	(1.1)	(1.3)	(1.2)	(1.3)	(1.0)	(0.7)	(0.7)	(0.4)	(0.3)	(0.5)	0.8 ± 0.3
D	(1.4)	(1.1)	(1.7)	(1.1)	(1.2)	(1.3)	4.6 ± 0.8	(1.0)	(0.7)	(0.7)	(0.4)	(0.3)	(0.5)	(0.4)
n	(1.4)	(1.1)	(1.6)	4.0 ± 0.8	(1.2)	3.5 ± 0.9	3.5 ± 0.9	(1.0)	(0.7)	(0.7)	(0.4)	(0.3)	(0.5)	(0.4)
H	(1.4)	(1.2)	(1.7)	(1.1)	(1.2)	(1.4)	(1.2)	(1.0)	1.4 ± 0.5	(0.7)	(0.4)	(0.3)	0.9 ± 0.3	0.9 ± 0.3
A	⋯	⋯	⋯	(5.1)	9.6 ± 3.8	(6.2)	(5.6)	7.7 ± 3.6	9.9 ± 2.1	(3.2)	⋯	9.9 ± 2.4	(2.2)	(2.0)
C	(35)	(33)	27.8 ± 3.7	12.7 ± 1.7	11.9 ± 1.9	11.3 ± 1.9	12.0 ± 1.8	19.5 ± 7.2	20.4 ± 7.4	15.8 ± 4.0	(20.8)	(16.0)	(18.0)	(17.4)
F	⋯	⋯	⋯	(5.4)	19.5 ± 4.1	57.9 ± 7.2	34.6 ± 5.5	40.1 ± 5.4	6.2 ± 2.6	8.6 ± 2.5	⋯	5.5 ± 1.5	20.0 ± 3.6	9.9 ± 2.6
G	⋯	⋯	⋯	(4.1)	(4.6)	(5.2)	(4.5)	(3.7)	(2.5)	(2.5)	(2.2)	5.7 ± 1.4	15.5 ± 2.7	(1.6)
E	(7.1)	(5.3)	(6.7)	(2.3)	(2.5)	(2.8)	7.1 ± 2.4	11.8 ± 3.1	(1.4)	(1.4)	(1.0)	(0.5)	(1.0)	(0.9)
15	(8.5)	(7.1)	(8.0)	(2.6)	5.9 ± 1.8	5.6 ± 2.6	(2.8)	(2.3)	3.0 ± 1.3	(1.6)	(1.2)	(0.6)	(1.1)	(1.0)
6	⋯	⋯	⋯	20.9 ± 3.9	24.5 ± 4.6	21.7 ± 4.1	33.2 ± 4.9	34.1 ± 5.6	7.0 ± 2.4	(3.2)	⋯	16.0 ± 3.6	37.9 ± 6.2	(2.0)
7	⋯	⋯	⋯	(4.1)	8.0 ± 3.1	23.8 ± 4.3	31.4 ± 4.7	20.7 ± 3.8	7.1 ± 2.2	(2.6)	11.9 ± 3.5	21.5 ± 4.7	14.8 ± 3.6	(1.6)
25	(8.9)	(7.3)	(8.2)	(2.6)	(2.9)	(3.1)	8.8 ± 2.0	(2.3)	6.3 ± 1.3	(1.6)	(1.2)	(0.6)	5.4 ± 1.2	19.2 ± 2.1
12	⋯	⋯	⋯	(3.1)	(3.5)	8.5 ± 2.9	11.2 ± 2.6	20.4 ± 2.7	(1.9)	38.3 ± 4.2	18.4 ± 4.3	13.4 ± 2.7	69.9 ± 7.1	2.8 ± 0.9
11	⋯	⋯	⋯	(4.8)	(5.3)	(5.9)	22.8 ± 4.7	(4.2)	12.6 ± 3.7	(2.9)	⋯	27.9 ± 6.5	11.9 ± 2.5	(1.8)
16	⋯	⋯	⋯	(5.9)	(6.5)	(7.2)	(6.4)	(5.2)	(3.6)	(3.6)	⋯	(1.1)	4.7 ± 1.6	(2.3)
5[b]	⋯	⋯	⋯	⋯	⋯	⋯	⋯	⋯	⋯	⋯	⋯	30.9 ± 7.5	⋯	⋯

Note. The values in parentheses correspond to 3σ upper limits.
[a] Integrated flux densities are presented in mJy.
[b] Source 5 is outside the FOV for all but the 2011 June 4 at 30.5 GHz, whose FOV is larger.

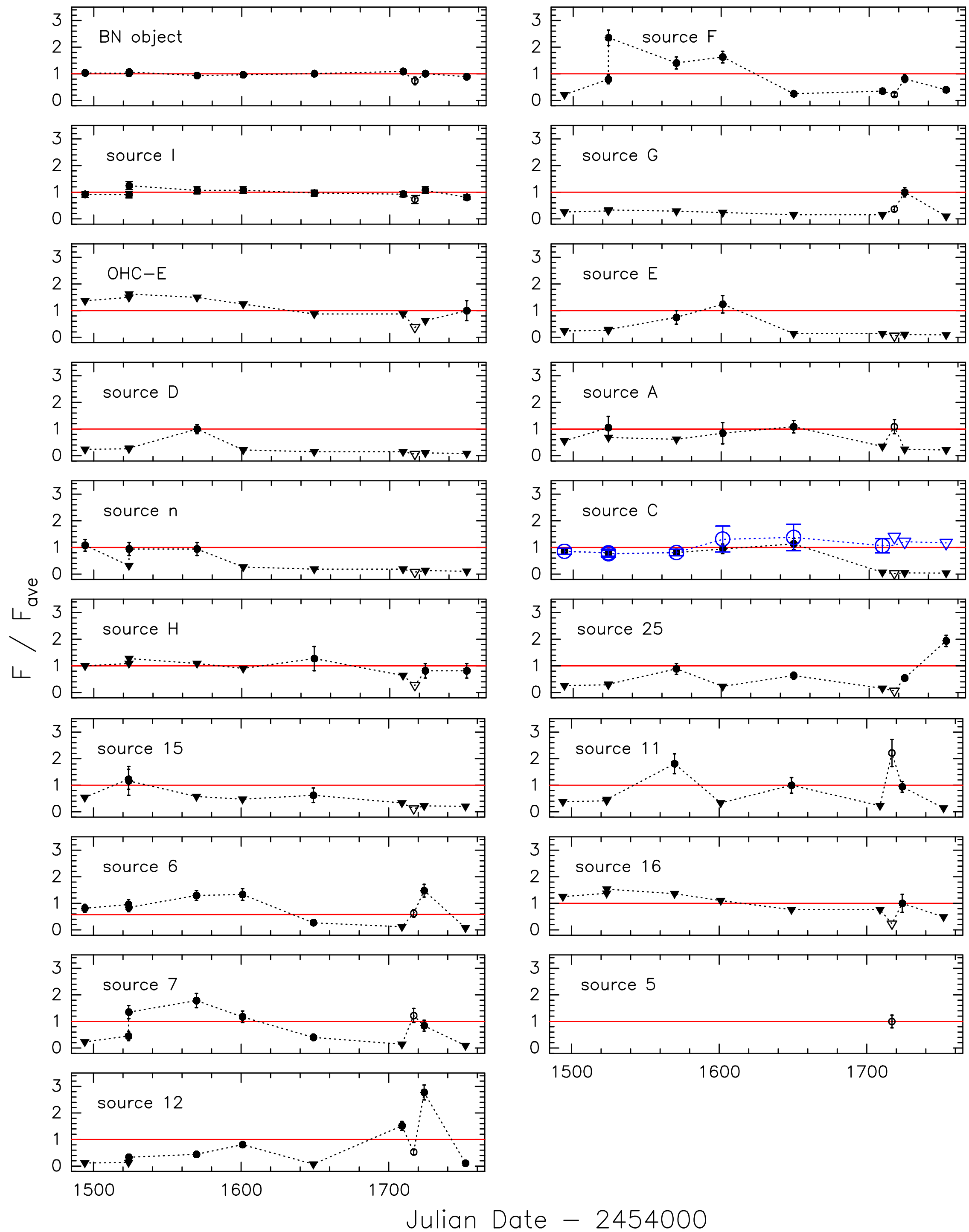

Figure 3. Ka-band light curves of all the 19 sources detected throughout the Ka-band monitoring. In the case of non-detections, 3σ upper limits are indicated with triangles. The flux densities have been normalized by the average value ($F_{\rm av}$) calculated with the positive detections (or the average value of the upper limits if the source is not detected). The error bars indicate the flux density uncertainties. The red horizontal line indicates the value at which the flux density is equal to the average flux density. The dotted line merely joins the flux densities at different epochs, and is not indicative of the evolution of the flux density between epochs. The frequency of the observations plotted is 33.6 GHz (black symbols), with the exception of the 2011 June 4 observation, which corresponds to a frequency of 30.5 GHz (indicated with open symbols). The second and third epoch on 2010 November 23 are only separated by ~3 hr. We discuss this short-term variability in detail in Section 3.2. For source C, the blue open symbols indicate values for extended emission derived from smoothed images (see Section 3.1).

2454000, and the variability parameter defined between these two epochs is β. The sources BN, C, 15, and 6 are nearly constant within the flux density uncertainties, with variations within a factor of 0.95–1.17 and $\beta < 0.11$. The latter two sources, however, exhibit clear variations at other epochs (see Figure 4).

The sources n, 7, F, and 12 show clear radio flares (see Figure 7), with flux density increases by factors $\geqslant$2.4 and variability parameters $\beta \geqslant 0.59$ (Table 5). Source A, a well-known radio flaring source (Bower et al. 2003; Zapata et al. 2004; Gómez et al. 2008), suffers a significant decrease of its flux density, being undetectable in the second image.

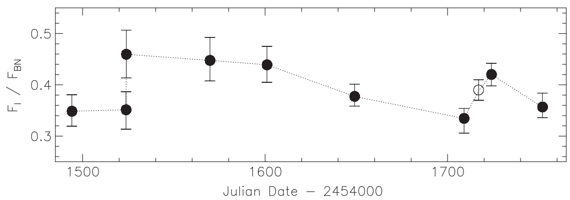

Figure 4. Ratio between the flux densities of sources I and BN vs. time at 33.6 GHz (filled circles) and at 30.5 GHz (open circle).

There is a tentative detection of variability in source I between the two epochs. The flux densities measured are not within the flux density uncertainty limits (see Figure 7 and Table 3), the variability parameter is $\beta = 0.22$, and the variation factor is 1.37 (while in the case of the BN source it is only 1.05). We conclude that this short-term variation of source I is not due to calibration uncertainties, and might be real. As already commented in Section 3.1, ionized gas of infalling accretion flows onto this massive star (Galván-Madrid et al. 2011; De Pree et al. 2014) might be responsible for the long-term variability observed in source I (Figure 5). However, other mechanism(s) would be needed to explain the variability observed in timescales of hours, like stochastic shocks in the radiative wind of the massive star (Stelzer et al. 2005), or the presence of an unseen low-mass companion emitting non-thermal gyrosynchrotron radiation. Indeed, Goddi et al. (2011) present arguments for source I harboring a binary system based on the kinematic history of the region. The interaction of a companion with the wind from a massive primary could explain the variability observed here.

3.3. Spectral Indices between 30.5 and 37.5 GHz

One of the methods commonly used to unveil the nature of the radio emission is studying the emission as a function of frequency, $F \propto \nu^{\alpha}$, where α is the spectral index.

In the 2011 June 4 observations, we have observed simultaneously at two different frequencies, 30.5 and 37.5 GHz. The calibration uncertainty in this epoch is higher than in the other runs (see Section 2), which implies large uncertainties in the derivation of α. However, it is worth mentioning that source 7 and source G exhibit clear flux decreases with $\alpha < -0.4$ (see Figure 8), suggesting that the dominant emission mechanism seems to be non-thermal.

4. COMPARISON WITH LOWER RADIO FREQUENCY AND CONNECTION TO X-RAY EMISSION

With the aim of better understanding the nature of the radio emission from young stars of the ONC/OMC region, in this section we compare the properties of the 33.6 GHz emission from our monitoring with those of the 8.3 GHz emission from Zapata et al. (2004). These authors analyzed VLA observations in four different epochs within a larger FOV and cadence ~1 yr. We have cross-correlated our sample of 18 radio sources emitting at 33.6 GHz with their catalog of radio sources.

Furthermore, to explore the link between the radio and X-ray emission in a statistically significant sample, we study the full sample of sources emitting at both wavelengths in Orion. We have cross-correlated the full sample radio sources with the catalog of X-ray stars provided by the very deep *Chandra* Orion Ultra Deep Project (COUP, Getman et al. 2005a).

The ONC/OMC region harbors different populations of radio stars: (i) members of the optically visible foreground ONC illuminated by the massive stars of the Trapezium (some of them associated with proplyds), (ii) stars still embedded in the background OMC in a earlier evolutionary stages, and (iii) extragalactic (EG) sources. Since the emission mechanisms of each group could be different, we distinguish in our study these different populations.

4.1. Source Membership

To obtain a rough estimate of the number of expected EG sources we follow Fomalont et al. (2002), who estimated the expected number of EG contaminants at 8 GHz. In a typical FOV at 8 GHz, the expected EG contamination is ~1 source (Zapata et al. 2004). In the smaller FOV of our 33.6 GHz monitoring, we would expect an even lower EG contamination of ~0.01 sources at 8 GHz for the most sensitive of our observations and a detection criterion of 5σ. Since these extragalactic sources generally show non-thermal emission of the type $F \propto \nu^{\alpha}$ with $\alpha < 0$ between 1 and 100 GHz (Condon 1992), the contamination at 33.6 GHz is expected to be even lower. We therefore conclude that the impact of EG contamination in our monitoring is very low. In the case of the Zapata et al. (2004) observations at 8.3 GHz, they inferred ~1 EG source.

We classify the radio sources into four groups: ONC members without evidence of proplyds ("naked" ONC), ONC members associated with proplyds, embedded OMC members, and EG contaminants. We cross-check the radio sources with available stellar catalogs in the optical (O'dell & Wen 1994; Hillenbrand 1997; Kastner et al. 2005), infrared (Hillenbrand & Carpenter 2000), and X-rays (COUP, Getman et al. 2005a). Additionally, we compare the position of the sources with the spatial distribution of the OMC, traced by the CN $N = 1$–0 emission from Rodriguez-Franco et al. (1998). A scheme explaining the method used to classify the sources is presented in Figure 9. It is based on six steps:

1. The presence of an optical counterpart indicates that the source is likely an ONC member. Since it is possible that some of the sources identified in this way are foreground field stars not related to the young cluster, we have additionally cross-correlated the radio sample with the list of 16 field stars from Getman et al. (2005b), without any coincidence.
2. The presence of IR counterpart indicates that the source is likely an ONC or OMC star, because EG sources are expected to be weaker IR sources.
3. The value of hydrogen column density N_H derived from X-rays is in general a good indicator to discriminate between ONC and OMC members. A source with log $N_H < 22.5$ cm^{-2} is considered an ONC member (Rivilla et al. 2013a).
4. The presence of X-ray variability is a good indicator to determine if a highly extincted source without an IR counterpart is an embedded OMC member or an EG source, because young stars are expected to exhibit much higher X-ray variability. Following Getman et al. (2005a) we consider three signposts of X-ray radio variability: (i) the significance of a Kolmogorov–Smirnov test (P_{KS}),

Table 4
List of Radio Sources in the ONC/OMC Region Considered in Our Analysis

Radio Sources								X-ray Sources								Optical[b]			IR[c]	Mem.[d]
ID		33.6 GHz			8.3 GHz			COUP	Properties											
Source	Z04[a]	F_{av} (mJy)	ΔF (mJy)	β	F_{av} (mJy)	ΔF (mJy)	β	ID	MedE (keV)	HR_1	$\log N_H$ (cm^{-2})	$\log P_{KS}$	BB Num	X-ray Flare?[e]	$\log L_X$ (erg s^{-1})	OW94	H97	K05 (propl.)	HC00	
I	19	10.0	1.3	0.13	0.64	0.23	0.36	-[f]	…	…	…	…	…	…	…	…	…	…	…	OMC
C[g]	14	14.8	3.7	0.25	4.97	1.61	0.32	…	…	…	-	…	…	…	…	…	y	y	y	ONC
16	53	4.7	1.7	0.36	3.14	0.43	0.14	…	…	…	…	…	…	…	…	y	…	…	…	ONC
5	61	…	…	…	15.88	0.26	0.02	…	…	…	…	…	…	…	…	y	y	y	y	ONC
BN	12	25.5	1.6	0.06	3.61	0.25	0.07	599b[h]	…	…	…	…	…	…	…	…	…	…	y	OMC
OHC-E	…	0.8	0.2	0.27	…	-	…	655	3.58	0.89	22.85 ± 0.01	−4.00	9	y	31.37	…	…	…	y	OMC
D	21	4.6	3.0	0.65	1.04	0.68	0.65	662	4.50	0.98	23.22 ± 0.03	−4.00	13	y	31.29	…	…	…	…	OMC
n	17	3.7	1.7	0.45	1.12	0.37	0.33	621	3.57	0.84	22.74 ± 0.01	−4.00	13	y	30.97	…	…	…	y	OMC
H	18	1.1	0.3	0.28	0.66	0.50	0.75	639	3.99	0.96	23.06 ± 0.04	−4.00	8	y	30.90	…	…	…	…	OMC
A	6	9.1	3.7	0.40	16.84	26.7	1.58	450	3.32	0.64	22.34 ± 0.03	−4.00	12	y	32.27	…	…	…	y	ONC
F	76	24.6	18.1	0.74	15.04	5.10	0.34	965	1.31	−0.63	21.25 ± 0.10	−4.00	2	n	31.89	-	y	…	y	ONC
G	73	15.5	9.8	0.63	2.48	2.09	0.84	932	1.29	−0.64	21.17 ± 0.09	−4.00	12	y	32.18	-	y	…	y	ONC
E	63	9.5	5.5	0.58	2.07	0.47	0.23	844	1.63	−0.50	22.01 ± 0.14	−0.96	1	y	29.22	…	y	y	y	ONC
15	49	4.8	2.3	0.48	4.35	0.83	0.19	766	1.58	−0.32	21.54 ± 0.03	−4.00	20	y	30.71	…	y	…	y	ONC
6	59	25.6	12.8	0.50	22.23	0.33	0.01	826	2.31	0.16	22.06 ± 0.04	−4.00	11	y	30.35	…	y	y	y	ONC
7	52	17.6	10.6	0.60	10.12	0.87	0.09	787	2.43	0.29	22.40 ± 0.04	−4.00	5	y	30.22	y	y	y	y	ONC
25	38	9.9	6.6	0.67	4.96	0.61	0.12	732	1.33	−0.60	20.99 ± 1.99	−4.00	23	y	32.35	…	y	…	y	ONC
12	41	25.2	24.6	0.98	12.09	7.89	0.65	745	1.33	−0.59	20.79 ± 0.08	−4.00	20	y	32.33	y	y	…	y	ONC
11	42	12.6	8.5	0.68	10.82	0.17	0.02	746	2.23	0.19	22.10 ± 0.55	−3.40	2	n	28.79	y	y	y	y	ONC
ORBS	…	…	…	…	…	…	…	647	5.20	1.00	23.51 ± 0.03	−4.00	8	y	30.93	…	…	…	…	OMC
…	1	…	…	…	2.84	0.12	0.04	229	4.05	0.98	22.96 ± 0.19	−0.05	1	n	29.28	…	…	…	…	EG
…	2	…	…	…	0.81	0.81	1.00	342	1.98	−0.01	22.21 ± 0.01	−4.00	31	y	31.32	…	y	…	y	ONC
…	7	…	…	…	0.78	0.42	0.54	510	4.75	1.00	23.54 ± 0.06	−2.59	3	y	31.26	…	…	…	…	OMC
…	9	…	…	…	0.48	0.27	0.56	530	5.23	0.98	23.50 ± 0.03	−4.00	2	(y)	30.75	…	…	…	…	OMC
…	16	…	…	…	0.33	0.18	0.56	625	4.81	0.98	23.42 ± 0.05	−4.00	4	y	30.95	…	…	…	…	OMC
…	31	…	…	…	0.20	0.08	0.42	699	1.51	−0.50	21.61 ± 0.11	−4.00	4	y	29.54	…	y	y	y	ONC
…	33	…	…	…	2.90	1.79	0.62	708	1.54	−0.36	21.46 ± 0.05	−4.00	10	y	30.19	…	y	…	y	ONC
…	34	…	…	…	5.66	0.59	0.10	717	1.55	−0.54	20.98 ± 0.70	−0.44	1	(y)	28.53	y	y	y	y	ONC
…	37	…	…	…	1.44	0.04	0.03	733	2.49	0.19	22.54 ± 0.23	−2.33	2	n	29.40	y	…	y	y	ONC
…	43	…	…	…	4.05	0.43	0.11	747	3.47	0.33	22.25 ± 0.35	−1.06	1	y	28.88	y	y	y	y	ONC
…	44	…	…	…	1.33	0.48	0.36	757	1.89	−0.17	22.45 ± 0.21	−0.64	1	(y)	29.01	y	…	y	y	ONC
…	45	…	…	…	6.03	0.58	0.10	758	1.66	−0.29	21.73 ± 0.02	−4.00	29	y	31.05	y	y	y	y	ONC
…	46	…	…	…	1.70	0.84	0.49	768	1.63	−0.33	21.52 ± 0.04	−4.00	4	y	30.27	y	y	y	y	ONC
…	54	…	…	…	1.02	0.61	0.60	800	1.93	−0.14	22.36 ± 0.21	−0.85	2	y	28.86	…	y	y	y	ONC
…	56	…	…	…	0.65	0.45	0.69	807	1.37	−0.60	21.43 ± 0.10	−4.00	7	y	29.73	…	y	y	y	ONC
…	58	…	…	…	1.58	0.16	0.10	820	3.64	0.95	22.86 ± 0.13	−4.00	3	y	30.07	y	…	y	y	ONC
…	60	…	…	…	3.12	0.41	0.13	827	1.63	−0.41	22.24 ± 0.03	−4.00	2	n	30.46	y	y	y	y	ONC
…	64	…	…	…	7.65	0.45	0.06	847	1.35	−0.64	21.62 ± 0.35	−2.00	1	(y)	29.22	y	y	y	y	ONC
…	65	…	…	…	3.82	0.18	0.05	855	1.96	−0.01	21.69 ± 0.09	−4.00	8	y	31.79	y	y	y	y	ONC
…	69	…	…	…	2.03	0.38	0.19	876	3.22	0.70	22.69 ± 0.06	−2.60	3	y	29.81	…	y	y	y	ONC
…	71	…	…	…	4.05	0.39	0.10	900	4.04	0.46	23.54 ± 0.46	−4.00	2	y	30.44	…	y	y	y	ONC

Table 4
(Continued)

Radio Sources								X-ray Sources								Optical[b]			IR[c]	Mem.[d]
ID		33.6 GHz			8.3 GHz			COUP	Properties											
Source	Z04[a]	F_{av} (mJy)	ΔF (mJy)	β	F_{av} (mJy)	ΔF (mJy)	β	ID	MedE (keV)	HR_1	$\log N_H$ (cm^{-2})	$\log P_{KS}$	BB Num	X-ray Flare?[e]	$\log L_X$ (erg s^{-1})	OW94	H97	K05 (propl.)	HC00	
⋯	75	⋯	⋯	⋯	0.43	0.14	0.33	955	1.70	−0.31	21.46 ± 0.19	−0.36	2	y	28.78	⋯	y	y	y	ONC
⋯	77	⋯	⋯	⋯	2.81	1.71	0.61	1130	1.23	−0.71	21.28 ± 0.14	−4.00	7	(y)	31.67	⋯	y	⋯	y	ONC
⋯	3	⋯	⋯	⋯	0.16	⋯	⋯	378	1.23	−0.66	21.11 ± 0.07	−4.00	5	y	30.20	⋯	y	⋯	y	ONC
⋯	4	⋯	⋯	-	0.30	⋯	⋯	394	1.20	−0.72	20.00 ± 1.65	−4.00	6	y	31.32	⋯	y	⋯	y	ONC
⋯	5	⋯	⋯	⋯	0.24	⋯	⋯	443	2.42	0.35	21.76 ± 0.39	−0.51	1	n	28.25	⋯	y	y	y	ONC
⋯	8	⋯	⋯	⋯	0.11	⋯	⋯	524	3.31	0.52	22.37 ± 0.31	−4.00	2	y	28.51	⋯	y	y	y	ONC
⋯	13	⋯	⋯	⋯	0.32	⋯	⋯	607	4.37	0.22	⋯	−0.05	1	n	⋯	⋯	⋯	⋯	⋯	OMC[i]
⋯	20	⋯	⋯	-	0.29	⋯	⋯	658	2.37	0.23	22.23 ± 2.62	−4.00	9	y	30.41	y	y	y	y	ONC
⋯	23	⋯	⋯	⋯	0.32	⋯	⋯	671	1.50	−0.52	21.83 ± 0.14	−2.20	3	y	29.21	y	y	⋯	y	ONC
⋯	28	⋯	⋯	⋯	0.34	⋯	⋯	690	3.72	0.82	22.70 ± 0.15	−4.00	2	y	29.31	y	⋯	y	⋯	ONC
⋯	29	⋯	⋯	⋯	0.24	⋯	⋯	689	1.32	−0.61	20.85 ± 0.15	−4.00	22	y	31.82	⋯	y	⋯	y	ONC
⋯	51	⋯	⋯	⋯	0.30	⋯	⋯	780	3.60	0.92	22.83 ± 0.03	−4.00	6	y	30.95	⋯	⋯	⋯	y	ONC[j]
⋯	66	⋯	⋯	⋯	0.32	⋯	⋯	856	1.47	−0.47	21.65 ± 0.02	−4.00	9	y	30.34	y	y	y	y	ONC
⋯	70	⋯	⋯	⋯	0.32	⋯	⋯	885	1.44	−0.50	21.61 ± 0.02	−4.00	7	y	30.33	⋯	y	⋯	y	ONC

[a] Source ID from Zapata et al. (2004).
[b] Optical association from the work of H97 (Hillenbrand 1997) and K05 (Kastner et al. 2005).
[c] Infrared association from the work of HC00 (Hillenbrand & Carpenter 2000).
[d] Source membership: OMC—Orion Molecular Cloud; ONC—Orion Nebula Cluster; EG—extragalactic.
[e] From visual inspection of the X-ray light curves published by Getman et al. (2005a). The parentheses denote that the detection is uncertain.
[f] Although X-ray emission from wind shocks would be expected from the massive star associated with source I, the non-detection by *Chandra* is likely due to the presence of a nearly edge-on disk (Matthews et al. 2010) that absorbs the X-ray emission.
[g] As discussed in Section 3.1, source C is filtered out by the more extended VLA configuration observations. To compute the average flux, the variability parameter and the number of detections at 33.6 GHz, we have considered the images after smoothing to a C-configuration resolution of 0.″8.
[h] The massive BN object has an X-ray counterpart, COUP 599b, much fainter than a low-mass companion located 0.″9 from BN, COUP 599a (Grosso et al. 2005).
[i] The radio source 13 identified by Zapata et al. (2004) does not have an optical or IR counterpart, but it has an X-ray counterpart (COUP 607) with a low number of counts, which prevent the derivation of N_H. Rivilla et al. (2013b) showed that this source is likely driving a molecular outflow in the OMC1-S region, and hence we classified it as a star embedded in the OMC.
[j] COUP 780 does not have optical counterpart and exhibits high extinction (log N_H= 22.83 cm^{-2}). Given its location, we propose that it is a particularly embedded ONC star that belongs to the Trapezium cluster surrounding the massive star θ^1 *Ori C* (Rivilla et al. 2013a), rather than an OMC member.

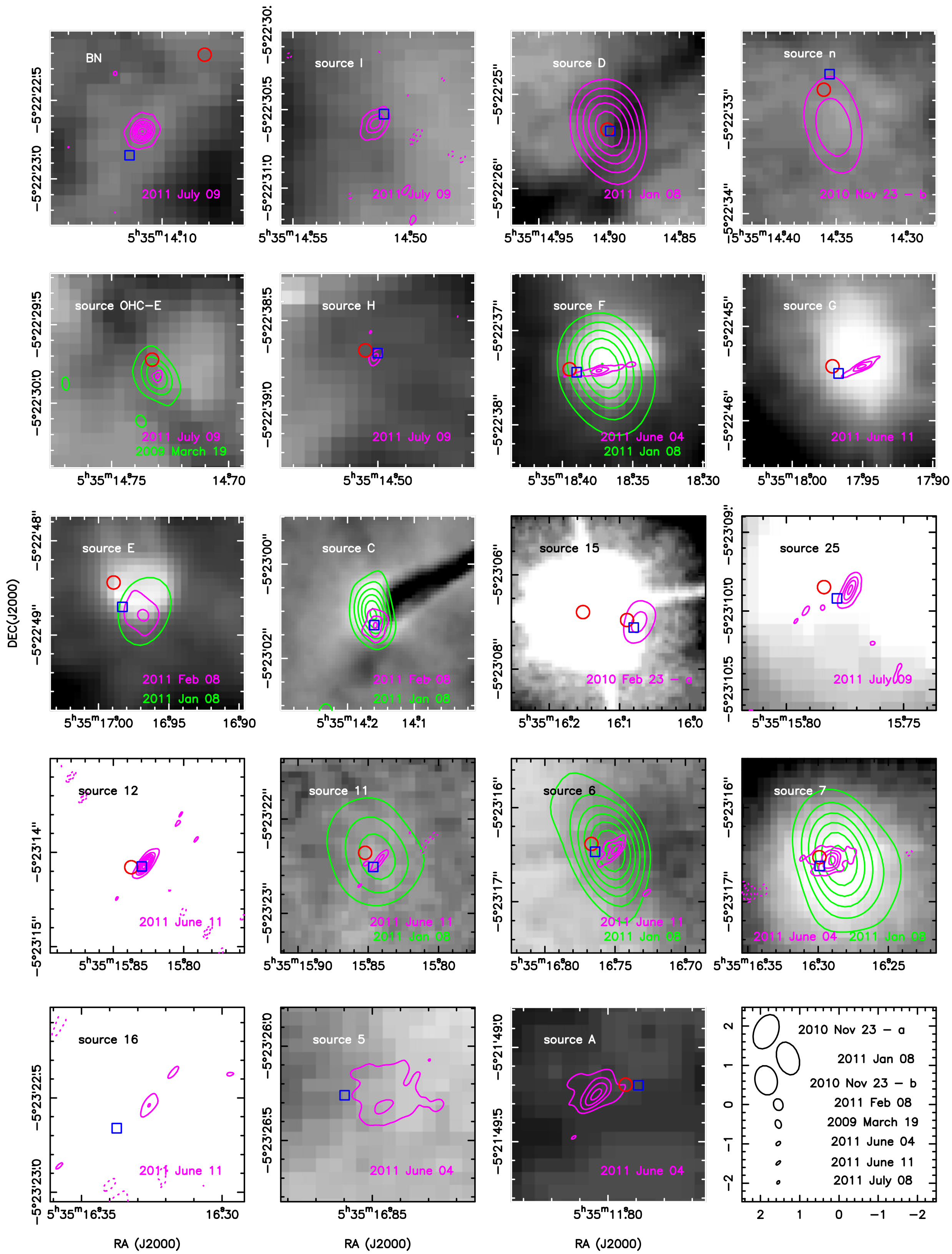

Figure 5. Images of the 19 radio sources detected in our radio monitoring. The name of the source is indicated in the top left corner of each panel. In the lower right corners we indicate the epoch of the observation (we have selected the epochs with the best spatial resolution and good detections, and in some cases we show the detections in two different epochs with different colors). The first contour level is 3σ and the step between successive contours is 2σ, with the exception of BN, I, 25, and 12 (which have steps of 10σ), and the 2009 March 19 epoch for OHC-E (steps of 5σ). The open blue squares indicate the position of known radio sources detected by Zapata et al. (2004) at 8.3 GHz, and the red circles denote the position of X-ray stars detected by *Chandra* (COUP Project). The background grayscale image is the ACS/WFC *HST* image at R-band, from the Hubble Legacy Archive. In the lower right panel we show the synthesized beams of the different images used.

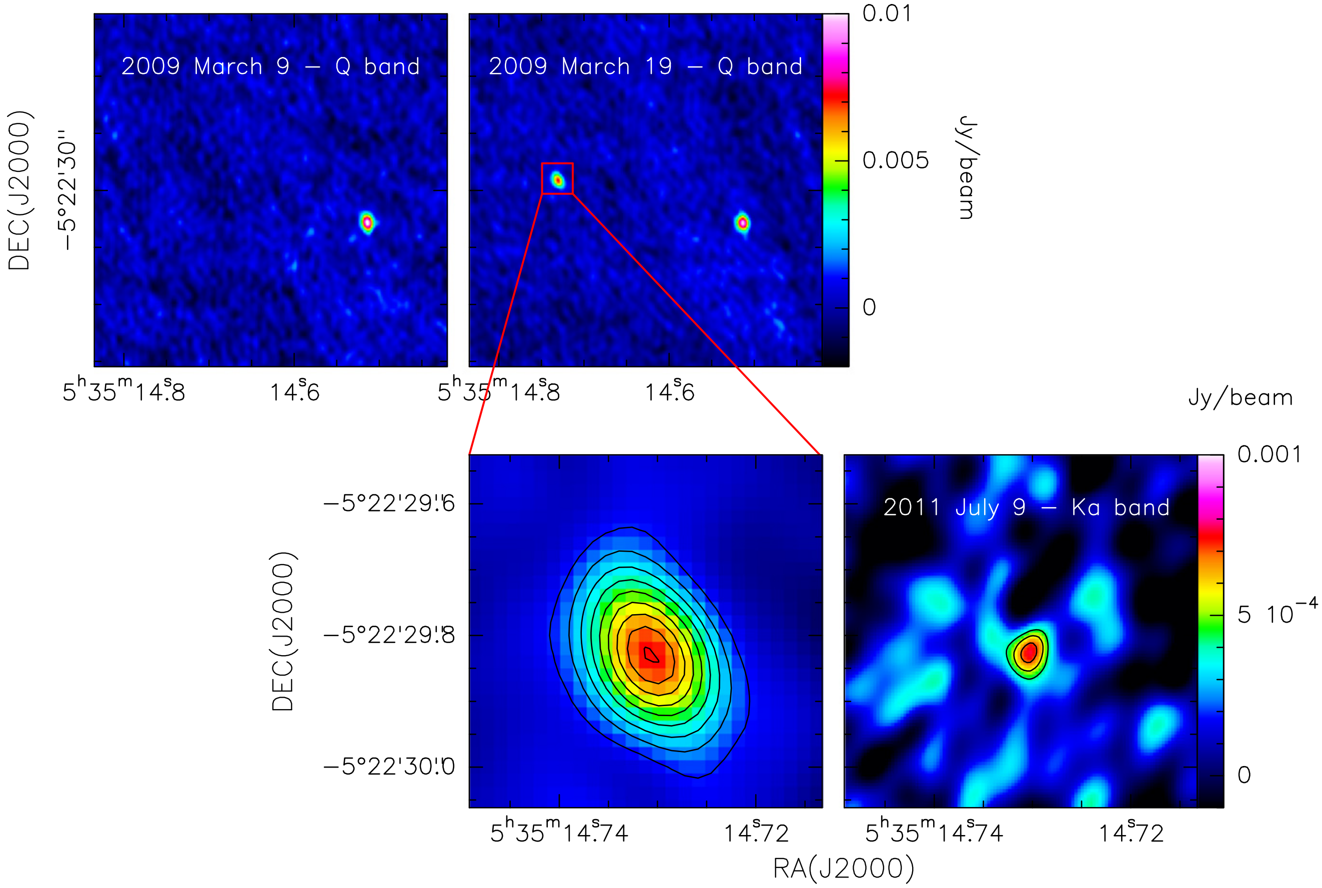

Figure 6. Upper panels: VLA observations of the OHC region at 45.6 GHz from 2009 March 9 (left) and 2009 March 19 (right). Source I is detected in both images, while the new radio flaring source OHC-E appeared 3″.3 toward the northeast on 2009 March 19. Lower left panel: zoom-in view of the detection of source OHC-E from the 2009 March 19 observation. The flux density scale is the same as in the upper panels. The contours indicate emission from 3σ to 19σ in steps of 2σ. Lower right panel: second detection of OHC-E in the 2011 July 9 observation. The contours indicate emission at 3σ, 4σ, and 5σ.

which establishes whether variations are above those expected from Poisson noise associated with a constant source, (ii) the number of segments of the Bayesian block parametric model (BBNum) of source variability developed by Scargle (1998), and (iii) visual inspection of the X-ray light curves. We consider that a source is X-ray variable when $P_{KS} < -2.0$ and/or BBNum $\geqslant 2$ and/or it exhibits X-ray flares in the light curves. We have obtained the values of P_{KS} and BBNum, and visually examined the X-ray light curves from Getman et al. (2005a) (see Table 4).

5. Finally, we compare the position of the sources with respect to the location of the OMC, traced by the CN $N = 1\text{–}0$ emission from Rodriguez-Franco et al. (1998; see the contours in Figure 10).

Additionally, to identify the ONC stars related to proplyds, we have cross-correlated the radio sample with the catalog of proplyds from Kastner et al. (2005), using a counterpart radius of 0″.5. The resulting membership classification is shown in the last column of Table 4. Figure 10 shows the spatial distribution of the different groups of sources.

4.2. Sample of Sources Emitting at 8.3 and 33.6 GHz

The cross-correlation between our radio sample at 33.6 GHz and the radio sample at 8.3 GHz, with a counterpart radius of 0″.5, shows that all the 33.6 GHz sources were also detected at 8.3 GHz, with the only exception of the new radio flaring source OHC-E. On the other hand, our monitoring did not detect emission from 25 sources from Zapata et al. (2004) located within our FOV. The radio properties at both radio frequencies are summarized in Table 4. In the left panel of Figure 11 we compare the average flux densities at both frequencies. We have distinguished "naked" ONC stars, ONC stars related to proplyds, and OMC stars. For those sources without 33.6 GHz detection, we have considered 3σ upper limits measured in our image with the best sensitivity.

In general, the radio sources detected by our monitoring exhibit higher 8.3 GHz flux densities than those undetected. This suggests that the non-detection at high frequency is likely due to lack of sensitivity.

With only one exception, the radio sources have higher average flux densities at 33.6 GHz. In the case of sources BN, I and C, we interpret that this is due to "quiescent" thermal component that increases with frequency. In the other sources, this does not directly imply evidence of thermal origin, because the observations are not simultaneous and their emission is highly variable (Section 3). Since this variability is likely connected to non-thermal processes, the value of F_{av} is very sensitive to the presence of flares, and not representative of their thermal emission.

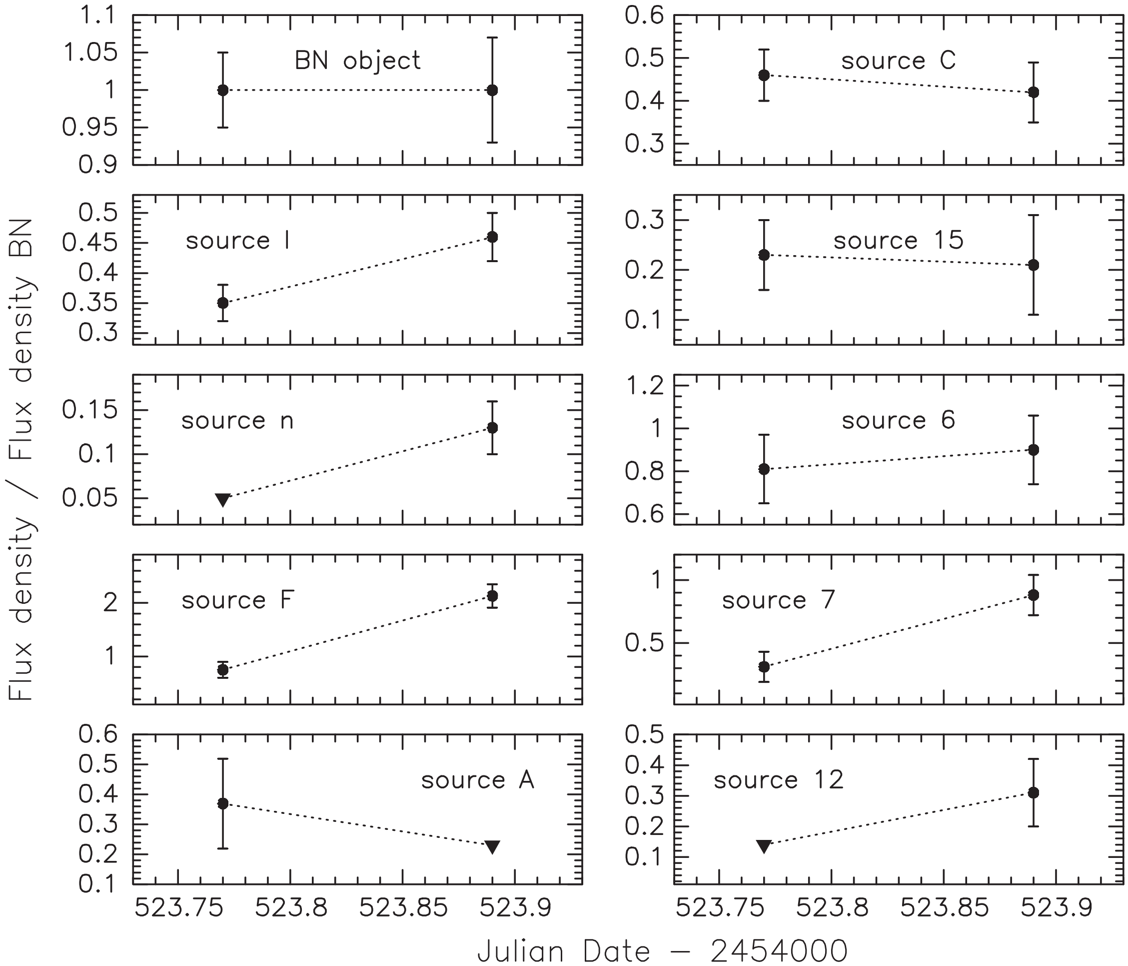

Figure 7. Flux density variation (normalized by the flux density of BN) on hour timescales for sources detected in the two runs observed on 2010 November 23.

Table 5
Radio Variability on Hour Timescales between the Two Observations on 2010 November 23

Source	$F_{523.89}/F_{523.76}$	β
BN	1.05	0.03
I	1.4	0.22
n	2.9	0.69
F	3.0	0.70
7	3.0	0.70
A	0.7	0.30
C	0.95	0.04
15	0.95	0.04
6	1.17	0.11
12	2.4	0.59

In the middle and right panels of Figure 11 we compare the values of ΔF and β at 8.3 and 33.6 GHz. Most of the sources appear more variable at higher frequencies (15/17 have higher ΔF; and 11/17 have higher β). This may indicate that the radio variability increase with frequency, although new observations of a more statistically representative sample of sources are needed to confirm this behavior.

We note that even the sources related to proplyds, which are expected to emit non-variable free–free or dust emission from circumstellar material, are clearly variable. This points toward the presence of a non-thermal component arising from the central PMS stars.

4.3. Full Sample of Sources Emitting Radio and X-rays

We have cross-correlated of the sample radio sources (detected at 8.3 GHz and/or at 33.6 GHz[13]) with the COUP catalog, searched for X-ray counterparts within 0″.5 of the radio sources. We have obtained a final sample of 51 sources emitting at radio and X-rays. The properties of the X-ray counterparts are shown in Table 4.

4.3.1. Radio Properties

In Figure 12 we show the radio properties of the subsamples of X-ray sources with emission at 8.3 and 33.6 GHz. The ONC sources related to proplyds exhibit low absolute variability at 8.3 GHz ($\Delta F \lesssim 1$ mJy) compared to "naked" ONC stars, which appear more variable ($\Delta F \gtrsim 1$ mJy). This suggests that the 8.3 GHz emission in the proplyds is dominated by thermal nearly constant emission from circumstellar material, while "naked" ONC stars are might be dominated by variable non-thermal processes related to magnetic activity of the PMS star. This could be gyrosynchrotron emission produced by the

[13] We have also included the flaring radio source ORBS detected by Forbrich et al. (2008) at 22 GHz.

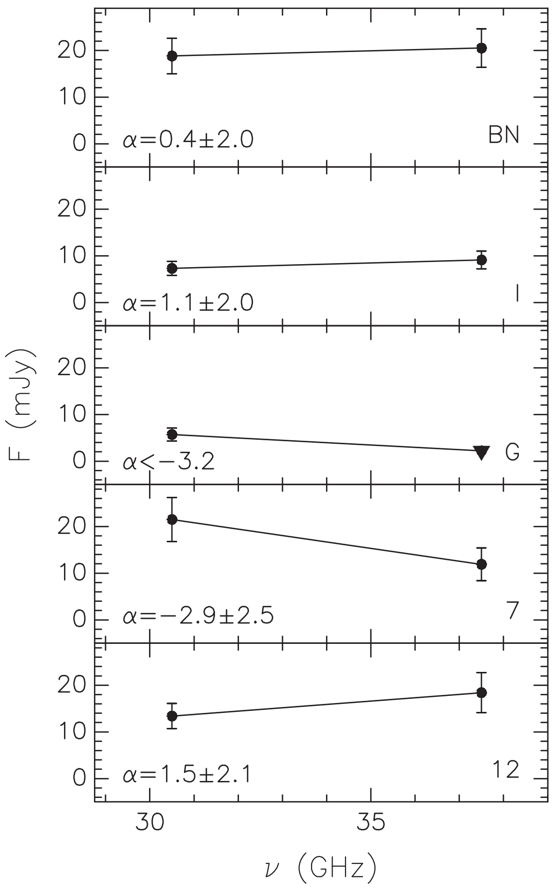

Figure 8. Flux densities at 30.5 and 37.5 GHz from the 2011 June 4 observations.

acceleration of electrons in magnetic field reconnection events in the corona of the star (Andre et al. 1996).

However, we note that most of the proplyds with lower F_{av} have values of $\beta > 0.1$ (left panel of Figure 12), because their ΔF is a significant fraction of their F_{av}. Therefore, it seems that the 8.3 GHz emission from proplyds, although dominated by thermal emission, could include also a non-thermal component arising from the central PMS stars.

The OMC members show low values of absolute variability at 8.3 GHz (ΔF < 1 mJy). However, since most of them are weak sources, this low absolute variation translates into significant relative variability, with values of $\beta > 0.1$, also pointing to non-thermal origin. Only BN is nearly constant, with low values of both ΔF and β, as occurs at 33.6 GHz. This confirms that the radio emission is likely dominated by thermal emission from the ionized gas in the massive envelope around the star.

The right panel of Figure 12 shows that all sources appear in general more variable at 33.6 GHz (both in ΔF and β). This may indicate that the emission at higher frequencies is more dominated by non-thermal highly variable processes.

Therefore, we conclude that the radio emission can be attributed to two different mechanisms: (i) highly variable (flaring) non-thermal radio gyrosynchrotron emission produced by accelerated electrons in the magnetospheres of low-mass PMS stellar members of both the ONC and OMC and (ii) non-variable thermal emission from the ionized gas and heated dust of the ONC proplyds illuminated by the Trapezium Cluster or from the ionized gas in the envelopes surrounding massive stars, as in the case of the BN object.

4.3.2. X-ray Properties

1. *Hydrogen column density N_H, hardness ratio (HR_1), and median energy (MedE)*: in Figure 13 the values of median energy (MedE) of X-ray photons and the hardness ratio[14] (HR_1) of the full radio/X-ray sample as a function of N_H are shown. It is clear that the stars embedded in the OMC have higher values (MedE >3.5 keV and HR_1 >0.84) than ONC stars. Feigelson et al. (2005) found a relation between the MedE of the X-ray photons arising from the stars and the hydrogen column density N_H (left panel of Figure 13). This trend is due to an absorption effect: in the embedded sources, only the harder photons are able to escape through the molecular gas and then be detectable, while softer ones (with lower energy) are absorbed. As a consequence, the embedded stars appear as harder sources. Among the ONC members, those related to proplyds exhibit higher values of N_H (and hence of MedE and HR_1). This is likely due to the presence of circumstellar material that produces higher extinction than in "naked" ONC stars.

2. *X-ray luminosities*: in Figure 14 we show the radio properties of the radio/X-ray sample as a function of the extinction-corrected X-ray luminosity L_X. We find that $L_X^{\text{ONC-proplyds}} < L_X^{\text{OMC}} < L_X^{\text{ONC-naked}}$. Although this result could be physically real, we note that it should be taken with caution, because the derivation of the extinction-corrected luminosity is more uncertain for highly extincted sources.

   We also investigate whether there is a relation between the radio properties and the X-ray luminosity in the radio/X-ray sample. Forbrich & Wolk (2013) remarked that there is no clear correlation between the radio flux densities measured by Zapata et al. (2004) at 8.3 GHz and the COUP X-ray luminosities (upper left panel in Figure 14). Similarly, we do not see a trend in our subsample at 33.6 GHz (upper right panel in Figure 14). However, if we do not consider the proplyds a tentative trend appears: the radio flux density generally increases with the X-ray luminosity. This suggests a relation between the X-ray and radio emissions for the "naked" ONC and OMC sources. In the case of proplyds, a significant fraction of radio emission is expected to arise from gas ionized by external illumination, which is not linked to X-ray activity. Therefore, a relation between the radio flux and X-ray luminosity is not expected in proplyds, as observed in Figure 14.

   We have also studied the fraction of X-ray sources detected at radio wavelengths as a function of the X-ray luminosity (Figure 15) for the 8.3 and 33.6 GHz monitorings. In each case, we have considered the COUP sources that fall within the FOV of each observation with enough counts so that the X-ray luminosity corrected for extinction could be reported. We find 159 X-ray sources within our FOV and 595 sources within the 8.3 GHz FOV. Both samples show a very similar behavior. The

[14] Hardness ratio $HR_1 = (h - s)/(h + s)$, where h and s refer to the counts detected in the hard (2.0–8.0 keV) and soft (0.5–2.0 keV) bands, respectively. Values closer to 1.0 indicate a hard X-ray source, and –1.0 a soft X-ray source.

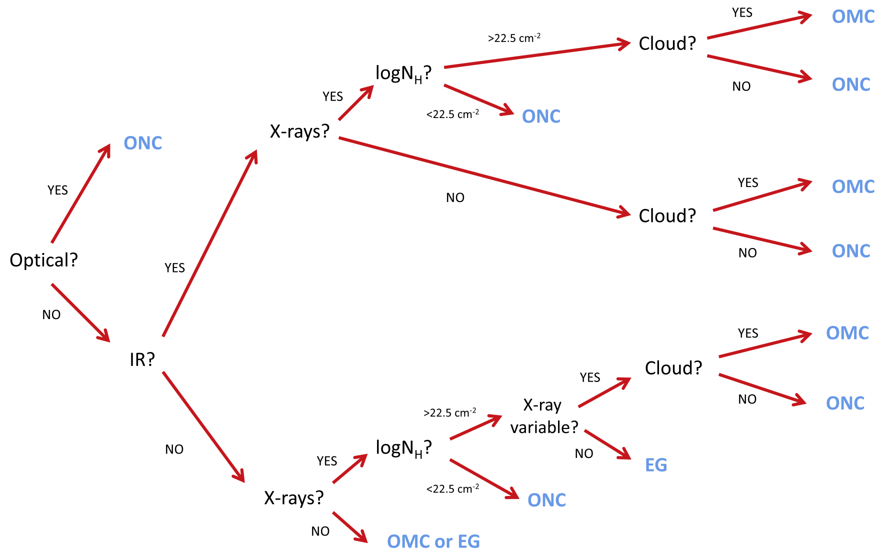

Figure 9. Scheme of the method used to classify the sources as ONC or OMC members, or EG sources. We use cross-correlation with optical, IR, and X-ray stellar catalogs, and compare with the spatial distribution of molecular material (see text).

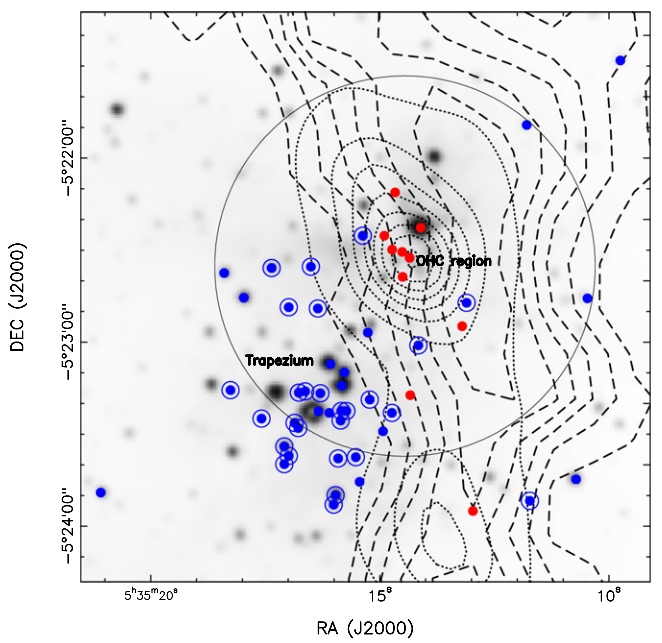

Figure 10. Spatial distribution of the full sample of sources used in our analysis. Red and blue dots indicate members of the ONC and OMC, respectively. The ONC sources related to proplyds are denoted by large blue circles. The radio source classified as EG falls outside the region shown. The gray scale shows the IR K-band image from the 2 Micron All Sky Survey (2MASS). The dashed contours trace gas from the OMC (CN N = 1–0 emission from Rodriguez-Franco et al. 1998), from 12 K km s^{-1} in steps of 4 K km s^{-1} . The dotted contours correspond to emission at 850 μm from Di Francesco et al. (2008). The large circle indicates the primary beam of the 33.6 GHz observations.

weaker X-ray sources with $\log L_X < 28.5$ erg s^{-1} (200 sources, i.e., 13% of the full COUP sample) were not detected by our radio monitoring, while Zapata et al. (2004) only detected one source. Figure 15 shows that the fraction of X-ray sources detected in the radio increases with X-ray luminosity. This indicates that the radio observations have statistically detected the most luminous X-ray sources. This suggests that (i) the underlying mechanisms responsible for the X-ray and (at least some fraction of) the radio emission are somehow related and (ii) radio monitorings have been limited in the past due to sensitivity, confirming the conclusion of Forbrich & Wolk (2013).

The middle and lower panels of Figure 14 also show tentative trends between the radio variability (ΔF and β) and the X-ray luminosity for the sources not related to proplyds. In general, the radio variability increases toward higher L_X.

However, we note that the number of sources of the "naked" ONC and OMC subsamples is too low to draw robust general conclusions. Deeper radio observations detecting a much larger number of sources are needed to confirm these tentative trends.

3. *X-ray variability*: we now study whether there is a relation between the radio and the X-ray variability. We follow the three conditions presented in Section 4.1 to consider a source X-ray variable: $P_{\rm KS} < -2.0$ and/or BBNum $\geqslant 2$ and/or presence of X-ray flares in the light curves (see Table 4). Only one radio source (E) of the 33.6 GHz/X-ray subsample does not exhibit X-ray variability. Namely, 93% of the stars of this subsample are X-ray variable. Regarding the full radio/X-ray sample, 85% of the stars are X-ray variable. These fractions are higher than the fraction of X-ray variable sources of the full COUP sample, which is ~60% (Getman et al. 2005a). Therefore, we have found that the radio sources are mostly associated with X-ray variable stars. This supports that (at least some of the) radio emission might be related to the same magnetic events in the coronae of PMS low-mass stars that also produce the X-ray emission.

In Figure 16 we show the radio properties of the radio/X-ray sample as a function of the level of X-ray variability, quantified by BBNum. As in Figure 14, tentative trends appear if we do not consider the proplyds. However, given that the X-ray and radio observations were carried out at different epochs and different sensitivities, no firm conclusions can be drawn. Unlike

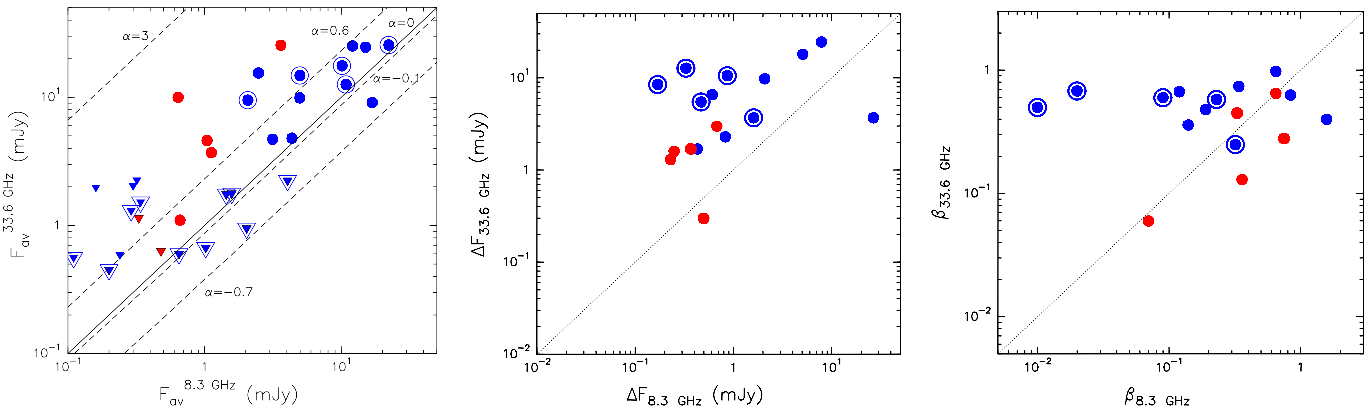

Figure 11. Comparison of radio properties at 33.6 and 8.3 GHz. Red and blue dots indicate members of the ONC and OMC, respectively. The ONC sources related to proplyds are denoted by large blue circles. Left panel: mean flux density at 33.6 GHz vs. the mean flux density at 8.3 GHz. For those sources that fall within the FOV of our 33.6 GHz observations but are only detected at 8.3 GHz, we have included 3σ upper limits (blue solid triangles; and large empty triangles if they are related to proplyds). The dashed lines show the relation expected for different types of emission: optically thin thermal dust (spectral index $\alpha \sim 3$); optically thick, ionized, stellar wind ($\alpha = 0.6$); optically thin free–free ($\alpha = -0.1$); and non-thermal synchrotron ($\alpha = -0.7$). We also indicate with a solid line the case of a flat spectrum ($\alpha = 0$). Middle panel: comparison between ΔF at 8.3 GHz and 33.6 GHz. The symbols are the same as in the left panel. Right panel: comparison between the variability parameters β at 8.3 and 33.6 GHz. The symbols are the same as in the left panel.

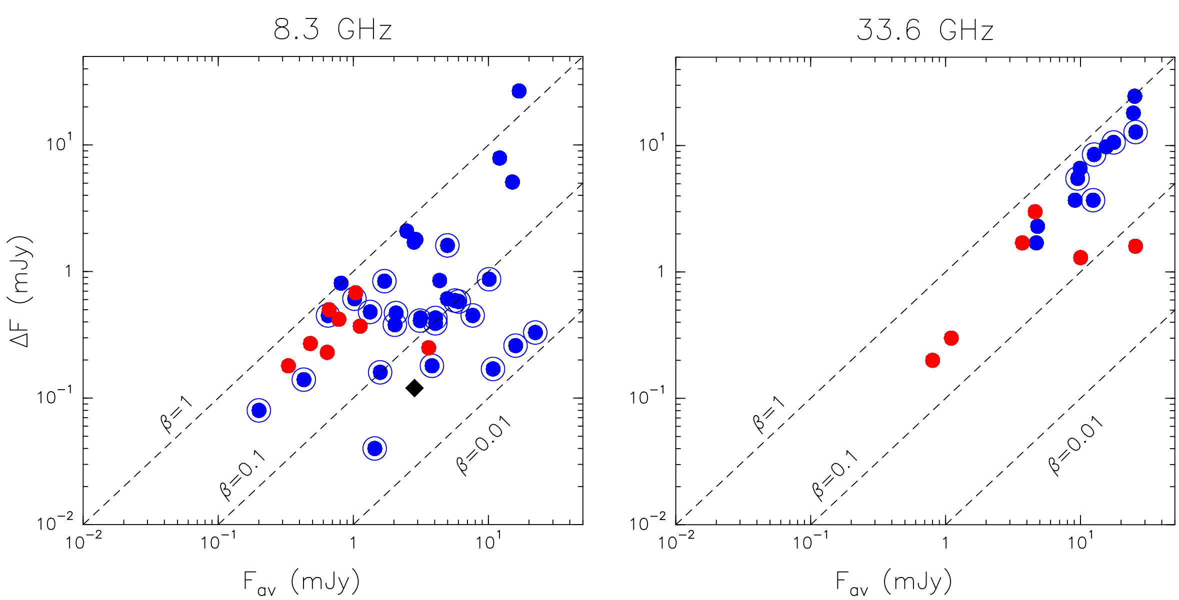

Figure 12. Radio properties at 8.3 GHz (left) and 33.6 GHz (right) of the radio/X-ray sample. The black diamond corresponds to the EG source. The other colors and symbols are the same as in Figure 10. The dashed lines indicate values of β of 1, 0.1 and 0.01.

the very deep COUP observation, which continuously observed the region during ~10 days, the radio monitoring runs are much shorter, yielding a lower probability to detect large flux density variations such as flares. To better understand if radio and X-ray variability are directly related, simultaneous observations will be needed.

5. THE NEW RADIO SOURCE EMBEDDED IN THE ORION HOT CORE: OHC-E

Our observations have detected twice a new radio source, OHC-E (2009 March 19 and 2011 July 09, see Figure 6). Neither Felli et al. (1993) nor Zapata et al. (2004), who performed observations covering seven months and four years at 5 and 15 and 8.3 GHz, respectively, nor Goddi et al. (2011), who observed the same region at 45 GHz two months before our detection (2009 January 12), detected emission toward this source.

The source is not resolved by the beam of our observations in any of our two detections (~0.″2 and ~0.″075). We can set upper limits to the deconvolved size of the emission of <0.″1 (<40 AU) for the Q-band emission and of <0.″04 (<10 AU) for the Ka-band emission. Unfortunately, it is not possible to determine the spectral index of the emission because observations at several radio wavelengths were not carried out simultaneously. We derived lower limits to the brightness temperature of ~460 and ~615 K from the source flux density at 45.6 and 33.6 GHz, respectively, and the upper limits to the source sizes. Although these temperatures are consistent with both thermal and non-thermal emission, our monitoring shows that the emission is highly variable, suggesting a non-thermal origin.

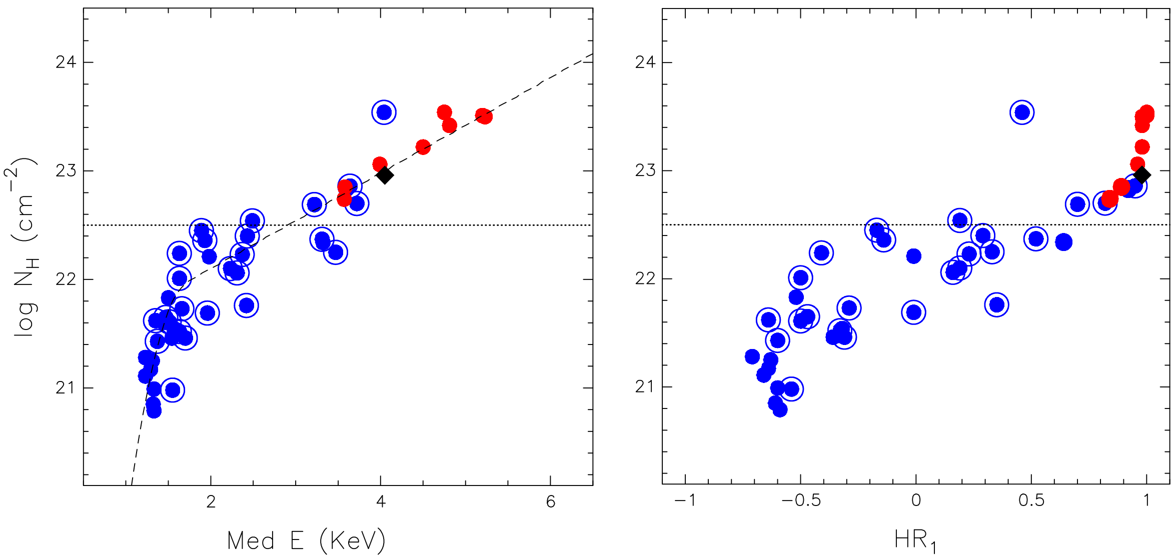

Figure 13. Relation between the hydrogen column density $N_{\rm H}$ and the median energy of X-ray photons (MedE, left panel) and the hardness ratio ($\rm HR_1$, right panel) of the members of the radio/X-ray sample. The dashed line in left panel is the empirical fit found by Feigelson et al. (2005). The colors and symbols are the same as in Figure 12.

The position of the radio flare coincides with an embedded X-ray low-mass PMS star COUP 655 (Figure 17). Source OHC-E is also located very close to the southeast member of a binary stellar system (CB4, Figure 17) observed with high angular resolution by the NICMOS on board *HST* (see also Stolovy et al. 1998; Simpson et al. 2006). Therefore it seems that both the radio and the X-ray emission are related to this star. We can give a rough estimate for the mass of this star using the canonical relation for X-ray young stars, $\log[L_X/L_{\rm bol}] = -3.0$ (Pallavicini et al. 1981). Assuming a stellar age typical for a massive star-forming region of 5×10^5 year, OHC-E would have a mass of $\sim 1\ M_\odot$ (using the Siess et al. 2000 stellar models), supporting that it is a low-mass star. Hence, the variability observed both in radio and X-rays wavelengths can be related to magnetic activity in the corona of this PMS low-mass star.

6. SOURCE 12: THE BINARY θ^1 ORI A

θ^1 Ori is a binary system, with a B0.5 primary and a low-mass eclipsing companion (Lohsen 1975). As observed in the binary WR 140 (Williams et al. 1990), the binarity can produce a smooth periodic variation of the radio emission caused by the combination of two geometrical effects: (i) variation of the free–free opacity due to the ionized envelope of the primary star as the companion orbits (ii) variation of the stellar activity (and hence the non-thermal emission) inversely proportional to the separation between components.

Felli et al. (1991, 1993) monitored the radio emission from this binary at 5 and 15 GHz. We plot in Figure 18 their flux densities and those of our monitoring as a function of the orbital phase ϕ. We have used the orbital parameters $P = 65.4325$ and $T_0 =$ JD 2446811.95 (Bossi et al. 1989). The flux density at 5 and 15 GHz peaks near periastron ($\phi \sim 0.15$), with lower levels at $\phi \sim 0.1$ and $\phi = 0.6$–0.9. Our higher frequency flux densities are consistent with those at lower frequencies, with a peak after periastron at $\phi \sim 0.2$. As Felli et al. (1993) noted and our data at higher frequency confirm, the orbital modulation model may cause the main peak to be detected always at the same position $\phi \sim 0.15$–0.2. However, the presence of large scatter in the radio emission cannot be explained with this model. Felli et al. (1993) set an upper limit for the variability timescale of 10–20 days. Our monitoring has revealed variability at shorter timescales of hours (Section 3.2). This is in agreement with non-thermal emission due to stellar activity, perhaps in addition to orbital modulation. Therefore, we conclude that although certain orbital modulation may be present, producing the observed flux density peak, there is also a non-thermal emission component arising likely from the low-mass companion that varies independently of the orbital phase.

7. RATE OF RADIO FLARING ACTIVITY

There are only a few radio flares detected from young stellar objects. This could indicate that these phenomena are rare events, or alternatively, that the sensitivity of the observations carried out so far has limited their detection. Our monitoring allows us to evaluate which is the most likely scenario. We have detected flares in sources OHC-E, F, n, 7, and 12. Other sources (e.g., D, E, G, 6, 11, 12, and 25) showing high levels of variability through different epochs separated by longer timescales, might be also flaring sources, but with our data we are not able to confirm short-term variability.

Bower et al. (2003) parametrized the rate of radio flares (flares day^{-1}) in the entire ONC/OMC region based on their data and the previous observations of variable sources by Felli et al. (1993). Since the number of flares depends on the FOV of a particular observation, and of the stellar density of the observed region, we reformulate the expression for the rate of radio flares, $N_{\rm RF}$, to

$$N_{\rm RF} = \gamma \left(\frac{F_{3\sigma}}{100\ {\rm mJy}} \right)^{\alpha} \left(\frac{A_{\rm FOV}}{A_{\rm tot}} \right) \left(\frac{\Sigma_{\rm FOV}}{\overline{\Sigma}} \right), \tag{1}$$

where $F_{3\sigma}$ is the threshold detection limit (considered as three times the rms of the observation), α is the spectral index of the emission, $A_{\rm FOV}$ and $A_{\rm tot}$ are the areas of the observed region and the full ONC/OMC region, respectively, and $\Sigma_{\rm FOV}$ and $\overline{\Sigma}$

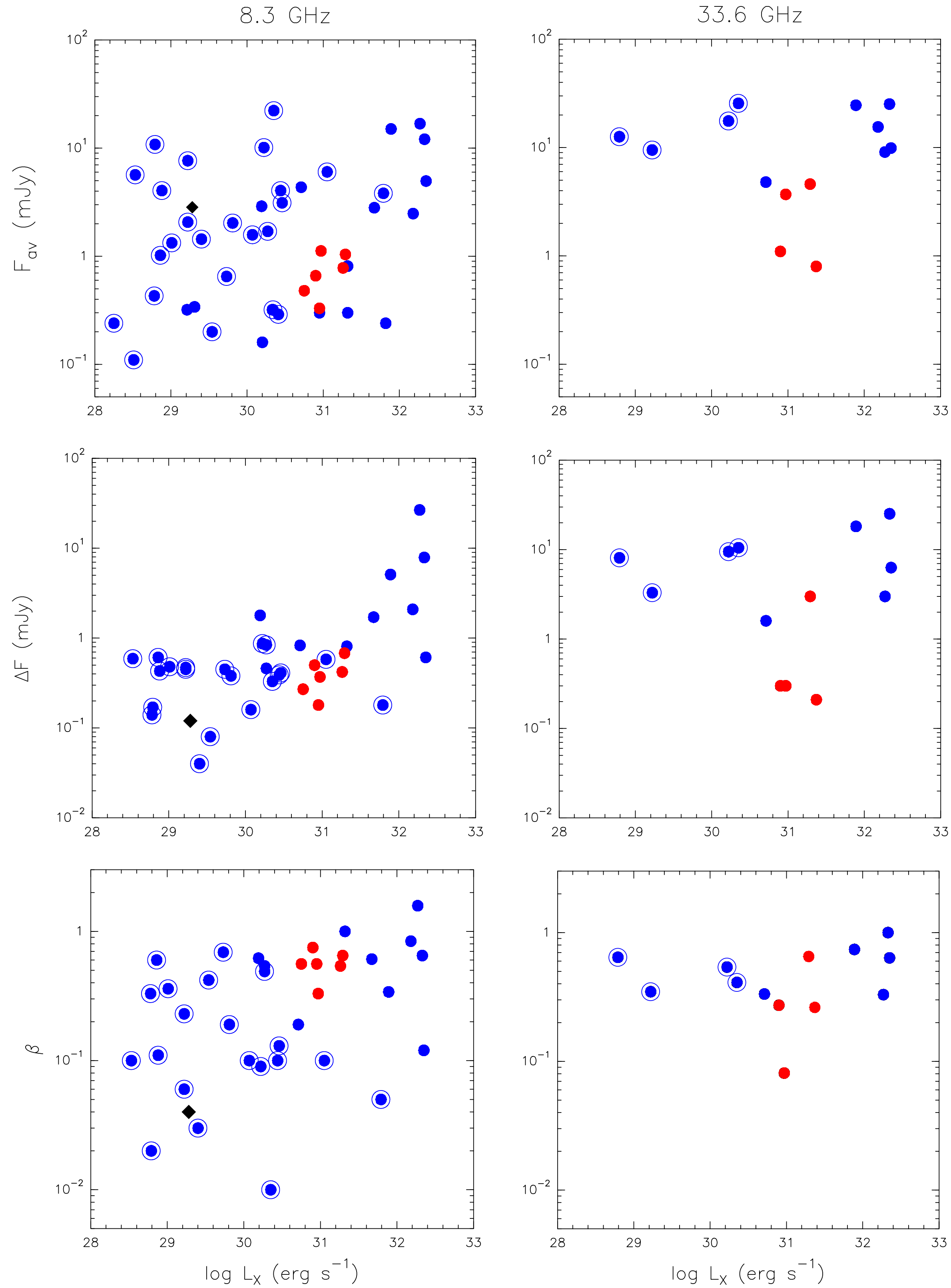

Figure 14. Radio properties ($F_{\rm av}$, ΔF, β) at 8.3 and 33.6 GHz vs. the value of the X-ray luminosity derived from the X-ray COUP counterparts. The colors and symbols are the same as in Figure 12.

are the surface stellar density in the observed region and the mean stellar density of the entire ONC/OMC, respectively. The parameter γ is a constant that Bower et al. (2003) estimated to be between 0.01 and 0.1.

Since the flare rate is a function of the stellar density, it is convenient to observe the more crowded region of a cluster to enhance the chances of detecting radio flares. The region with highest stellar density in Orion is the OHC (Rivilla

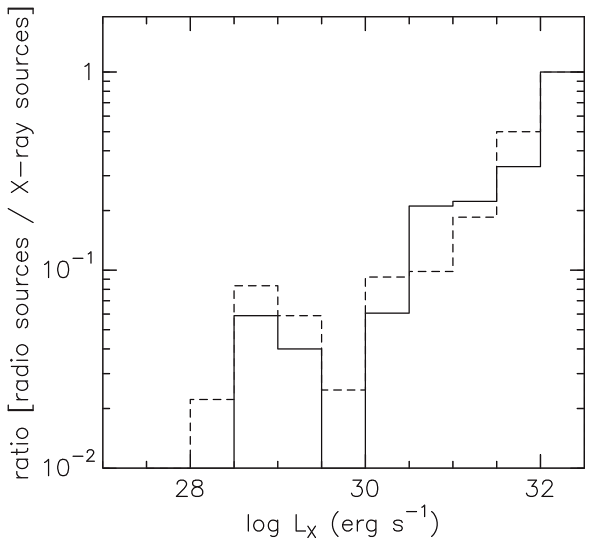

Figure 15. Fraction of X-ray COUP sources detected by our radio monitoring at 33.6 GHz (solid line) and Zapata et al. (2004) monitoring at 8.3 GHz (dashed line) as a function of the absorption-corrected total X-ray luminosity L_X. In each case, we have considered the COUP sources that fall within the FOV and with enough counts so that the X-ray luminosity corrected for extinction could be reported: 159 for our monitoring and 595 for the 8.3 GHz monitoring (see also Forbrich & Wolk 2013).

et al. 2013a). Considering a $\sim 25'' \times 25''$ region centered in the stellar density peak, using the typical power-law index of non-thermal emission of $\alpha = -1$, the mean rms noise of our monitoring (0.3 mJy), the approximated size of the ONC/OMC cluster of 15 pc × 15 pc, and the census of stars in the region provided by COUP, we obtained that $N_{\rm RF} \sim 0.017$–0.17 flares day^{-1}.

We have detected two clear flares (OHC-E and source n.)[15] in this area in 14 observations, so a rough estimate of the flaring rate is ~0.14 flare observation^{-1}. Assuming that the typical duration of the radio flares is several hours to days (Andre et al. 1996; Bower et al. 2003; Forbrich et al. 2008), this would be approximately equivalent to 0.14 flares day^{-1}, which is similar to the upper value from Equation (1). Therefore, our results suggest that γ is closer to 0.1 rather than to 0.01, and consequently that the number of detectable flares is significant. Therefore, our multi-epoch monitoring confirms that the presence of radio flares is not a rare phenomenon in crowded young stellar clusters.

Obviously, the detection of radio flares in the OHC is favored by its high density of embedded low-mass stars. But, according to Equation (1), even in less dense regions the number of detectable flares would be significant, especially if the sensitivity is enhanced. The improved capabilities of the VLA and ALMA may be expected to reveal many more radio flares arising from young low-mass star clusters. A single polarization ALMA observation at 90 GHz (band 3) with a full bandwidth of 7.5 GHz and 50 antennas, which can reach a 8 μJy sensitivity limit in only 2.3 hr of on-source observing time[16] considering an FOV of $\sim 25'' \times 25''$, this ALMA observation may find ~ 6 radio flares day^{-1}, which represents ~25% of the X-ray sources detected by *Chandra* in the region. This would confirm that radio flares are common events, similarly to the X-ray flares detected by *Chandra*.

Future observations are clearly needed to derive a better estimate of this radio flaring rate through the detection of many more radio flares. The flaring information for tens or even hundreds of PMS stars will provide a complete statistical description of radio short-term variability. Beyond the purely scientific interest, this would have important technical implications for interferometric imaging (Bower et al. 2003). The classical interferometric imaging techniques assume a constant sky in image reconstruction. However, this assumption would be violated by the presence of many variable sources in the field. This would lead to a reduced dynamic range of the image (Stewart et al. 2011). Also, it would become difficult to concatenate multiple observations of the same region to obtain deeper images. Therefore, a more accurate determination of the radio flare rate would help us understand to what extent this may affect deeper VLA and ALMA observations of young stellar clusters.

8. SUMMARY AND CONCLUSIONS

In this work we have presented a multi-epoch radio monitoring of the ONC/OMC region carried out with the VLA at high centimeter frequencies (33 and 45 GHz). We have detected 19 radio sources, mainly concentrated in the OHC and Trapezium regions. Two of them are related to massive stars: sources BN and I. The flux densities of the BN source and source C (related to a proplyd) are compatible with constant thermal emission. Source I, besides a constant thermal component, shows tentative evidence of radio variability at both short- and long-term timescales. The remaining 16 sources show long-term (month-timescale) variability, but it is not yet clear whether these comprise multiple short-term events not covered by our monitoring cadence. Indeed, we have confirmed radio flares (i.e., short-term radio variability on timescales of hours to days) in five sources: F, 7, n, 12, and the new source OHC-E, previously undetected at radio wavelengths.

We have complemented our radio sample with other radio detections at 8.3 GHz from the literature, and cross-correlated it with the X-ray COUP catalog to obtain the full sample of sources emitting radio and X-ray in the ONC/OMC region. The radio emission from young stars can be explained by a combination of two different mechanisms: (i) non-variable thermal emission produced by ionized gas and/or heated dust from the ONC proplyds and the massive objects BN and I and (ii) variable (flaring) non-thermal gyrosynchrotron emission produced by accelerated electrons in the stellar corona of PMS low-mass members of the ONC and OMC. We have found several hints relating this variable radio emission with the X-ray activity.

Our study of the radio variability of θ^1 Ori A concludes that there is evidence of a non-thermal emission component arising likely from the low-mass companion. Moreover, certain orbital modulation may be present in this binary, producing the observed flux density peak.

We have derived a rough estimate of the radio flaring rate in the densest cluster in the region, which is embedded in the OHC. We have obtained ~0.14 flares day^{-1}. This value is consistent with an empirical estimate assuming the sensitivity and FOV of our observations and the stellar density of the region. This confirms that radio flares are not rare phenomena

[15] The detections of sources H and D in the OHC region show also tentative evidences of flaring emission toward these stars (see Section 4.2).

[16] According to the ALMA sensitivity calculator available in the ALMA Observing Tool.

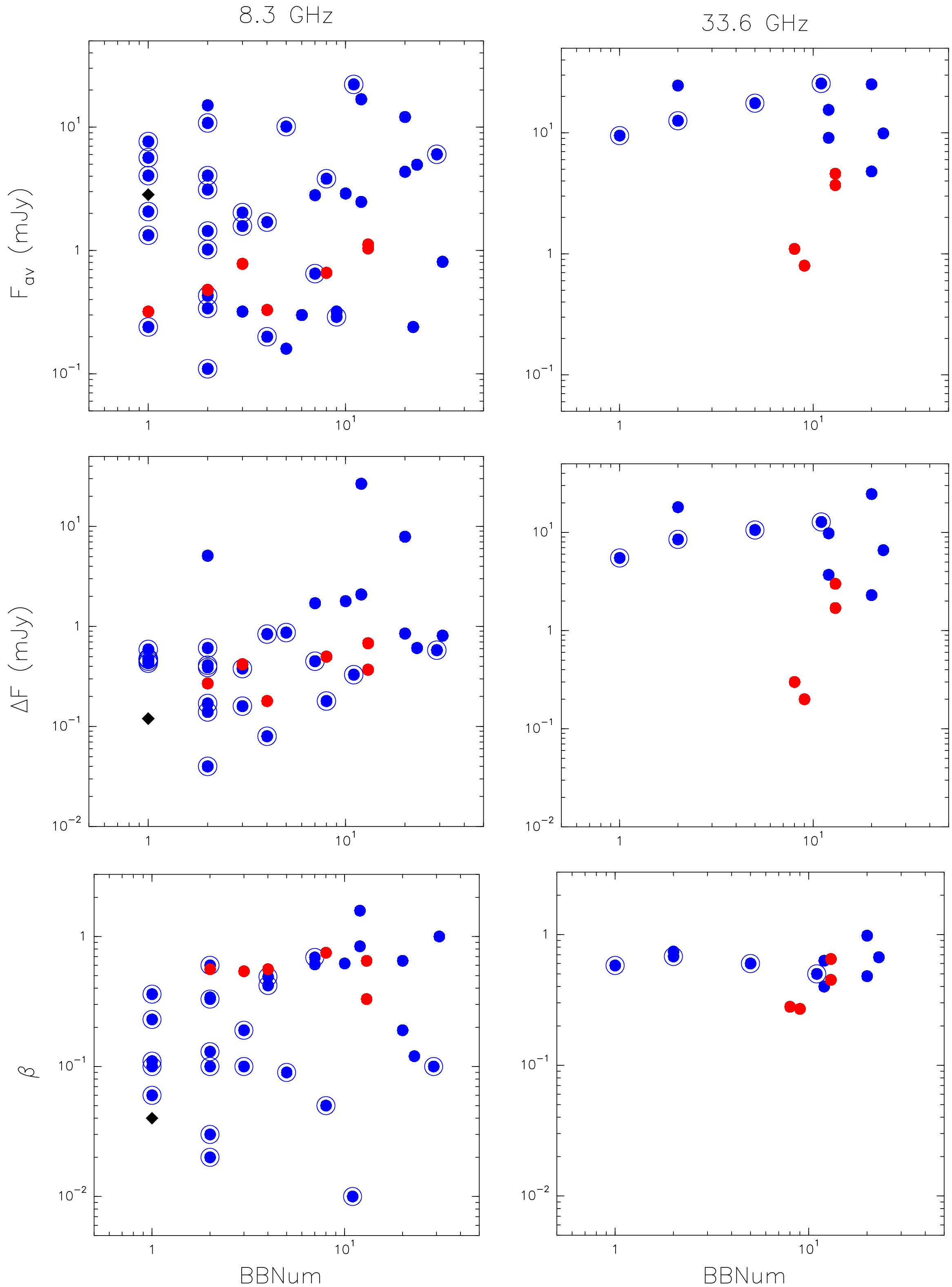

Figure 16. Radio properties (F_{av}, ΔF, β) at 8.3 and 33.6 GHz vs. the value of the BBNum derived from the X-ray COUP counterparts, which is a proxy for the X-ray variability. The colors and symbols are the same as in Figure 12.

during the earliest stages of star formation as previously thought, but relatively common events similar to the well-known X-rays flares.

Our results have shown that the radio monitorings to date has been strongly limited by sensitivity, detecting mainly those sources with higher X-ray luminosity. This implies that the new capabilities of VLA and ALMA offer a unique opportunity to detect a much larger population of radio sources in young stellar clusters. New observations with improved sensitivity and better angular resolution will provide crucial information about the origin and nature of the radio emission, and they will reveal how radio and X-ray phenomena are connected.

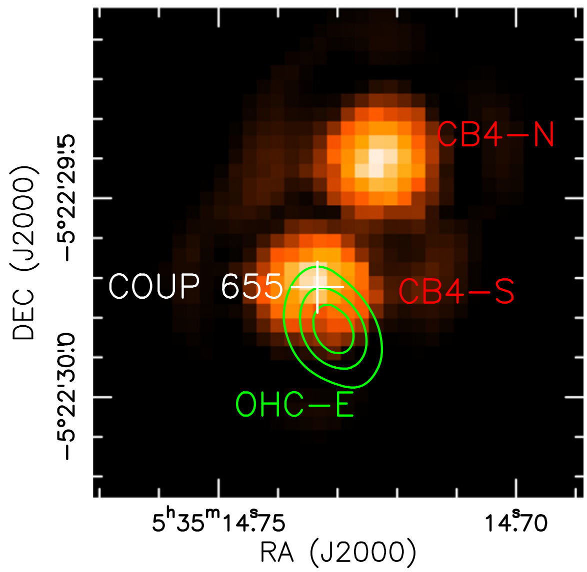

Figure 17. 2.15 μm *HST*-NICMOS image (color scale) of the region where OHC-E was detected, from the Hubble Legacy Archive (HLA). An IR binary is detected toward this region, CB4 (see also Stolovy et al. 1998; Simpson et al. 2006). The green contours correspond to the radio emission at 45.6 GHz detected on our 2009 March 19 image (5σ, 10σ, and 15σ). The positions of the X-ray star COUP 655 is indicated with the white plus sign.

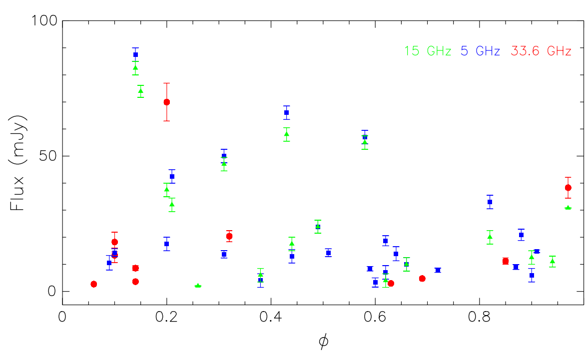

Figure 18. Flux densities of source 12 as a function of the orbital period at 33.6 GHz (red dots, this paper), and 5 and 15 GHz (blue squares and green triangles, respectively, from Felli et al. 1991, 1993).

Furthermore, the presence of multiple variable radio sources would have important implications for interferometric imaging, since the classical techniques assume a constant sky. A more accurate determination of the radio flare rate would help to understand how this variability can affect the upcoming VLA and ALMA observations in young stellar clusters.

This work has been partially funded by Spanish projects AYA2010-21697-C05-01 and FIS2012-39162-C06-01, and Astro-Madrid (CAM S2009/ESP-1496), and CSIC grant JAE-Predoc2008. I.J.-S. acknowledges the funding received from the People Programme (Marie Curie Actions) of the European Union's Seventh Framework Programme (FP7/2007-2013) under REA grant agreement number PIIF-GA-2011-301538. J.S.-F. acknowledges the funding received from the project AYA2011-30147-C03-03. The National Radio Astronomy Observatory is a facility of the National Science Foundation operated under cooperative agreement by Associated Universities, Inc.

REFERENCES

Andre, P. 1996, in ASP Conf. Ser. 93, Radio Emission from the Stars and the Sun, ed. A. R. Taylor & J. M. Paredes (San Francisco, CA: ASP), 273
Arzner, K., Güdel, M., Briggs, K., Telleschi, A., & Audard, M. 2007, A&A, 468, 477
Bossi, M., Gaspani, A., Scardia, M., & Tadini, M. 1989, A&A, 222, 117
Bower, G. C., Plambeck, R. L., Bolatto, A., et al. 2003, ApJ, 598, 1140
Choi, M., Hamaguchi, K., Lee, J.-E., & Tatematsu, K. 2008, ApJ, 687, 406
Close, L. M., Males, J. R., Morzinski, K., et al. 2013, ApJ, 774, 94
Condon, J. J. 1992, ARA&A, 30, 575
De Pree, C. G., Peters, T., Mac Low, M. M., et al. 2014, ApJL, 781, L36
Di Francesco, J., Johnstone, D., Kirk, H., MacKenzie, T., & Ledwosinska, E. 2008, ApJS, 175, 277
Drake, S. A., & Linsky, J. L. 1989, AJ, 98, 1831
Feigelson, E. D., Getman, K., Townsley, L., et al. 2005, ApJS, 160, 379
Feigelson, E. D., & Montmerle, T. 1999, ARA&A, 37, 363
Felli, M., Massi, M., & Catarzi, M. 1991, A&A, 248, 453
Felli, M., Taylor, G. B., Catarzi, M., Churchwell, E., & Kurtz, S. 1993, A&AS, 101, 127
Fomalont, E. B., Kellermann, K. I., Partridge, R. B., Windhorst, R. A., & Richards, E. A. 2002, AJ, 123, 2402
Forbrich, J., Menten, K. M., & Reid, M. J. 2008, A&A, 477, 267
Forbrich, J., Preibisch, T., Menten, K. M., et al. 2007, A&A, 464, 1003
Forbrich, J., & Wolk, S. J. 2013, A&A, 551, A56
Galván-Madrid, R., Peters, T., Keto, E. R., et al. 2011, MNRAS, 416, 1033
Garay, G. 1987, RMxAA, 14, 489
Getman, K. V., Feigelson, E. D., Grosso, N., et al. 2005b, ApJS, 160, 353
Getman, K. V., Feigelson, E. D., Micela, G., et al. 2008, ApJ, 688, 437
Getman, K. V., Flaccomio, E., Broos, P. S., et al. 2005a, ApJS, 160, 319
Goddi, C., Humphreys, E. M. L., Greenhill, L. J., Chandler, C. J., & Matthews, L. D. 2011, ApJ, 728, 15
Gómez, L., Rodríguez, L. F., Loinard, L., et al. 2008, ApJ, 685, 333
Grosso, N., Feigelson, E. D., Getman, K. V., et al. 2005, ApJS, 160, 530
Güdel, M. 2002, ARA&A, 40, 217
Hillenbrand, L. A. 1997, AJ, 113, 1733
Hillenbrand, L. A., & Carpenter, J. M. 2000, ApJ, 540, 236
Kastner, J. H., Franz, G., Grosso, N., et al. 2005, ApJS, 160, 511
Liu, H. B., Galván-Madrid, R., Forbrich, J., et al. 2014, ApJ, 780, 155
Matthews, L. D., Greenhill, L. J., Goddi, C., et al. 2010, ApJ, 708, 80
Menten, K. M., & Reid, M. J. 1995, ApJL, 445, L157
Menten, K. M., Reid, M. J., Forbrich, J., & Brunthaler, A. 2007, A&A, 474, 515
O'dell, C. R., & Wen, Z. 1994, ApJ, 436, 194
Pallavicini, R., Golub, L., Rosner, R., et al. 1981, ApJ, 248, 279
Plambeck, R. L., Bolatto, A. D., Carpenter, J. M., et al. 2013, ApJ, 765, 40
Reid, M. J., Menten, K. M., Greenhill, L. J., & Chandler, C. J. 2007, ApJ, 664, 950
Rivilla, V. M., Martín-Pintado, J., Jiménez-Serra, I., & Rodríguez-Franco, A. 2013a, A&A, 554, A48
Rivilla, V. M., Martín-Pintado, J., Sanz-Forcada, J., Jiménez-Serra, I., & Rodríguez-Franco, A. 2013b, MNRAS, 434, 2313
Rodriguez-Franco, A., Martin-Pintado, J., & Fuente, A. 1998, A&A, 329, 1097
Scargle, J. D. 1998, ApJ, 504, 405
Siess, L., Dufour, E., & Forestini, M. 2000, A&A, 358, 593
Simpson, J. P., Colgan, S. W. J., Erickson, E. F., Burton, M. G., & Schultz, A. S. B. 2006, ApJ, 642, 339
Stelzer, B., Flaccomio, E., Montmerle, T., et al. 2005, ApJS, 160, 557
Stewart, I. M., Fenech, D. M., & Muxlow, T. W. B. 2011, A&A, 535, A81
Stolovy, S. R., Burton, M. G., Erickson, E. F., et al. 1998, ApJL, 492, L151
Williams, P. M., van der Hucht, K. A., Pollock, A. M. T., et al. 1990, MNRAS, 243, 662
Wolk, S. J., Harnden, F. R., Jr., Flaccomio, E., et al. 2005, ApJS, 160, 423
Zapata, L. A., Rodríguez, L. F., Kurtz, S. E., & O'Dell, C. R. 2004, AJ, 127, 2252